Molybdenum reduction in a sulfidic lake: Evidence from X-ray absorption fine-structure spectroscopy and implications for the Mo paleoproxy

Tais W. Dahl [a,*,1], Anthony Chappaz [b,c,1], Jeffrey P. Fitts [d,e], Timothy W. Lyons [f]

[a] Nordic Center for Earth Evolution (NordCEE) and Institute of Biology, University of Southern Denmark, Campusvej 55,
DK-5230 Odense M, Denmark
[b] Institute for Great Lakes Research, Department of Chemistry, Central Michigan University, Mount Pleasant, MI 48859, USA
[c] Institute for Great Lakes Research, Department of Earth and Atmospheric Sciences, Central Michigan University, Mount Pleasant,
MI 48859, USA
[d] Department of Civil & Environmental Engineering, Princeton University, Princeton, NJ 08544, USA
[e] Environmental Sciences Department, Brookhaven National Laboratory, Upton, NY 11973-5000, USA
[f] Department of Earth Sciences, University of California, Riverside, CA 92521, USA

Abstract

Marine euxinic sediments, particularly organic-rich black shales, are important sinks for oceanic molybdenum (Mo), and the determination of Mo concentration and isotopic composition are used to constrain oxygenation state and specifically expansion of marine anoxic and sulfidic (euxinic) waters in ancient oceans. The use of Mo as a paleo-redox tracer is based on its distinct geochemical behavior in oxic and sulfidic environments. Mo removal from sulfidic waters starts with MoO_4^{2-} reacting with aqueous H_2S to form particle reactive thiomolybdates, $MoO_{4-x}S_x^{2-}$, but the post-thiomolybdate steps and the ultimate Mo host in euxinic sediments are not well understood. We used X-ray absorption fine structure (XAFS) spectroscopy to determine the oxidation state and the molecular coordination environment of pristine, solid phase Mo in sediments from permanently euxinic Lake Cadagno, Switzerland. Samples were taken from a 9-meter piston core representing the last ten thousand years of deposition.

The euxinic lake sediments provide unequivocal evidence that the post-thiomolybdate steps along the burial pathway involve Mo(VI) reduction to Mo(IV) before it is ultimately hosted in the sediments. Anoxic samples contain Mo(IV)–S compounds that, when oxidized upon air-exposure, are transformed into Mo(VI)–O, thus confirming our results. This observation is important to better understand the Mo burial pathway from oxic waters to euxinic sediments. Our results support a model where post-thiomolybdate Mo^{VI} reduction proceeds via reactions with zero-valent sulfur, S(0) (mainly S_8, Vorlicek et al., 2004). In this model, Mo is scavenged from sulfidic waters as reactive Mo-polysulfide species, $Mo(IV)O(S_4)S^{2-}$ or $Mo(IV)S(S_4)S^{2-}$, and not as thiomolybdate ($MoOS_3^{2-}$ or MoS_4^{2-}) as has been previously assumed. This result can have important implications for how paleoenvironmental redox conditions are inferred from sedimentary Mo enrichments, Mo/TOC ratios, and $\delta^{98}Mo$, if the Mo accumulation rate is accelerated via the S_8-assisted pathway in settings where partial oxidation of S is possible. For example, euxinic Mo/TOC ratios are predicted not only as a function of Mo concentration in overlying seawater. Instead, the ratio will be higher in sediments deposited under highly sulfidic waters where S_8 is also abundant, such as in settings where the chemocline depth fluctuates considerably and/or oxygen intrusions occur to the overlying

---

* Corresponding author. Tel.: +45 6550 2795; fax: +45 6550 2786.

E-mail address: tais.dahl@snm.ku.dk (T.W. Dahl).

[1] Both authors contributed equally to this work.

bottom waters. Partial oxidation of dissolved sulfide is an important step in polysulfide production. Finally, we conclude that XAFS measurements are a powerful way to study the Mo burial pathway in sediments and enhance our ability to infer past environmental conditions from the sedimentary record.

1. INTRODUCTION

1.1. The molybdenum redox proxy

Molybdenum (Mo) is a redox sensitive trace metal that can provide information on Earth's global ocean oxygenation over geological time (Arnold et al., 2004; Wille et al., 2007; Pearce et al., 2008; Scott et al., 2008; Dahl et al., 2010b, 2011). Methods include both elemental and isotopic measurements of geological records (mainly black shales), and their predictive power lies with an understanding of the chemical burial pathway from the ocean to the sediments. Here, we provide a first study of the Mo redox chemistry in a highly sulfidic Swiss lake from which we can infer governing reactions involved in the Mo enrichment process that are likely to be broadly relevant.

In oxygenated waters, Mo shows a conservative behavior with a long residence time of ~440–800 thousand years in modern oceans (Morford and Emerson, 1999; Miller et al., 2011). Mo is predicted to exist in its most oxidized state as tetrahedrally coordinated molybdate anion, $Mo(VI)O_4^{2-}$. In oxic waters, Mo adsorbs onto Fe/Mn-oxyhydroxides and can be preserved in lacustrine and marine oxic sediments, ferromanganese crusts, and Mn nodules (Shimmield and Price, 1986; Zheng et al., 2000; Chappaz et al., 2008). In contrast, under anoxic/sulfidic conditions MoO_4^{2-} reacts with H_2S to form thiomolybdates, $MoO_{4-x}S_x^{2-}$ (Erickson and Helz, 2000). Mo is removed from natural sulfidic waters and porewaters (Emerson and Huested, 1991; Zheng et al., 2000; Morford et al., 2007). However, the mechanistic processes involved in its ultimate sequestration into the sediments remain elusive. Particularly, the particle reactive Mo species have never been determined directly, i.e., the dissolved Mo species that adsorb onto or complex with particulate matter. Earlier workers suggested that a reduction step from Mo(VI) to Mo(IV) was necessary to fix Mo into sediments as MoS_2 (Francois, 1988; Emerson and Huested, 1991; Calvert and Pedersen, 1993), but later studies showed that MoS_2 is not the final Mo host in euxinic sediments (Helz et al., 1996; Bostick et al., 2003; this study). Mo scavenging from sulfidic water is more recently argued to be associated with precipitation of iron sulfides (Bostick et al., 2003; Helz et al., 2004, 2011; Vorlicek et al., 2004) and/or organic matter (e.g., Tribovillard et al., 2004; Algeo and Lyons, 2006). Recent advances in Mo speciation analyses showed that Mo(V) forms in pore fluids during anoxic incubation experiments under increasing sulfide concentrations (Wang et al., 2011). Despite these efforts, there is still no unified model for the steps governing Mo removal and thus sediment enrichment in sulfidic settings.

All current uses of Mo redox proxies (Mo, Mo/Al, Mo/TOC, $\delta^{98}Mo$) are founded on Mo's distinct geochemical behavior in oxic vs. anoxic/sulfidic environments (Crusius et al., 1996; Arnold et al., 2004; Algeo and Lyons, 2006) without specific knowledge of Mo speciation (oxidation state and coordination environment) and burial mechanisms in sulfidic environments. These uncertainties may limit the full potential of Mo as an indicator of past redox conditions, particularly if additional factors beyond dissolved sulfide and molybdenum availability control the enrichment process in some euxinic settings and/or induce isotope fractionation between sediments and seawater (Helz et al. 2011). Ultimately, better understanding of the enrichment pathways may enhance the utility of the proxy. One possibility is that Mo reduction is an important step in the removal process, with zero-valent sulfur playing a critical role of donating electrons (Vorlicek et al., 2004). Here, X-ray absorption fine-structure (XAFS) measurements were used to study Mo oxidation state and bonding environment in modern euxinic sediments. In a pioneering study of Mo using XAFS, Helz et al. (1996) studied Mo chemical structure in Phanerozoic black shales and concluded that it is coordinated to both O and S with a mean oxidation state between +4 and +6. They further suggested that Fe was present in the molecular coordination environment surrounding each Mo atom. In the present study, this approach is expanded by analyzing euxinic sediments deposited over the last ~10,000 years to explore the Mo redox state and molecular environment and how these change over this time scale of diagenesis.

1.2. XAFS principles

XAFS is uniquely suited to studying the atomic- and molecular-scale structure around chosen elements contained within a liquid or solid material. The principle of XAFS analysis can be summarized as follows. A given atom absorbs an X-ray photon, and the energy of the X-ray is transferred to a core-level electron (K shell for our experiment), which is ejected from the atom. The emitted 'photo-electron' wave scatters from the atoms around the X-ray absorbing atom, creating interferences. These quantum interference effects cause an energy-dependent variation in the X-ray absorption probability, which is proportional to the X-ray absorption coefficient. Modulations of the absorption spectrum provide information about the structure, oxidation state, neighboring atoms, bond lengths, and coordination number. XAFS spectroscopy consists of two complementary techniques (Fig. 1): X-ray Absorption Near Edge Structure (XANES) and Extended X-ray Absorption Fine Structure (EXAFS). EXAFS provides information on interatomic distances, coordination number, and type of nearest atoms to the Mo atom, while XANES is sensitive to oxidation state, ligand type, presence of Mo=O double bonds, and coordina-
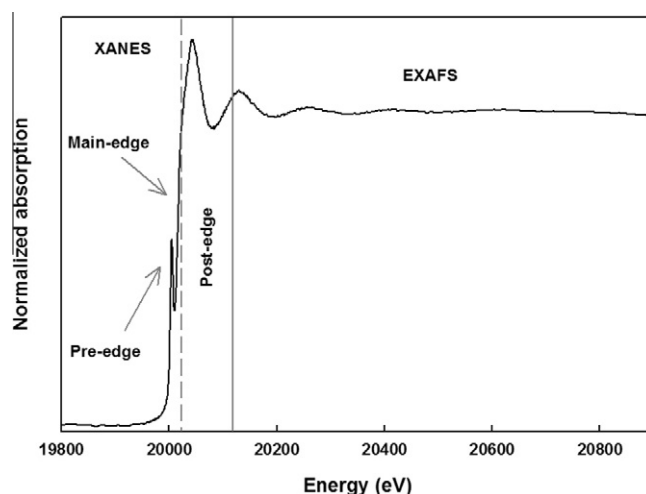
Fig. 1. XAFS Mo K-edge (20000 eV) spectrum of $Mo(VI)O_4^{2-}$. The XANES spectrum is subdivided into three regions. Pre-edge feature (-50 eV to K-edge) appears because s $\rightarrow$ d transitions are formally forbidden by dipole selection rules, while s $\rightarrow$ p transitions are allowed. A distinct pre-peak occurs with Mo=O double bonds typically associated with a high Mo oxidation state. The main absorption edge (E_K) is used to infer mean oxidation state. In the post-edge of the XANES spectrum (from 10 to $\sim$60 eV above K-edge) X-ray radiation absorbed by multiple scattering resonances (MSR) with neighboring atoms provides useful information about neighbor type and arrangement (Bianconi, 1988, p. 609). The EXAFS region (from $\sim$150 to $\sim$900 eV above K-edge) and ab initio model fit elucidate the type and bond lengths to atoms neighboring the Mo atom.

tion chemistry of the Mo atom (e.g., octahedral vs. tetrahedral coordination). Several publications are available for more detailed descriptions of the XAFS techniques, e.g., Rehr and Albers (2000) and Stern (1988).

2. METHODS

2.1. Site description

Lago di Cadagno is located at 1921 m altitude in the southern part of central Switzerland (Fig. 2). The lake is permanently stratified with oxic waters at <11 m depth overlying anoxic and sulfidic (euxinic) waters up to 21 m depth. The stratification is established by a density difference between heavy, solute-rich waters supplied through cold, subaquatic springs into the deeper part of the lake and river discharge of lower density fresh water into the surface layer. The local bedrock consists of felsic gneiss, dolomite, and gypsum. Sulfate delivered through subaquatic springs ($\sim$7 mM) is used by sulfate reducing bacteria to produce up to 300 µM hydrogen sulfide in the water column (Del Don et al., 2001).

Molybdenum is supplied to the lake through both the rivers and subaquatic springs in roughly equal proportions (Dahl et al., 2010a). It enters as soluble $Mo(VI)O_4^{2-}$ and reacts in a series of steps with H_2S to form thiomolybdates ($Mo^{VI}O_{4-x}S_x^{2-}$) in the euxinic zone. Thermodynamic calculations predict a geochemical switchpoint, $[H_2S_{aq}] > 11$-µM at which molybdate is no longer stable and sulfidation proceeds towards tetrathiomolybdate (Erickson and Helz, 2000). The post-thiomolybdate reactions are still not known, but Mo is bound to particulate matter in the sulfidic water column in Lake Cadagno and is delivered to and buried in sediments via the settling particles (Dahl et al., 2010a). Ultimately, this process yields strong Mo
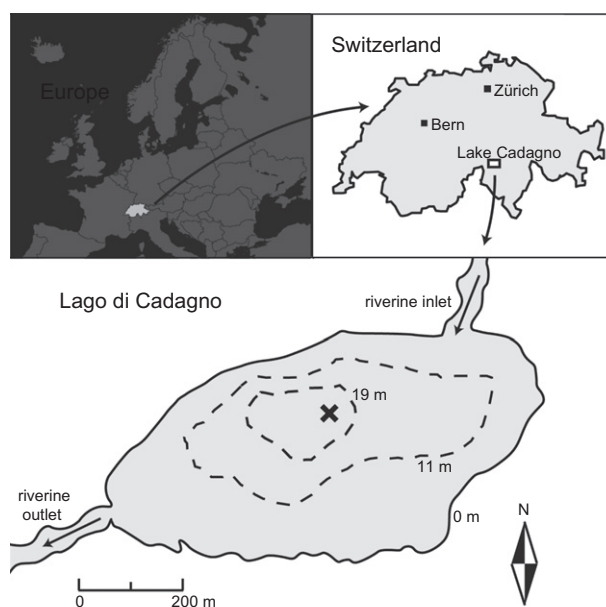

Fig. 2. Geographical and bathymetric map of Lago di Cadagno in Switzerland. The drill sites were located near the deepest part of the lake (marked with 'X').

enrichment in the sediments ($\sim$130 ppm) relative to felsic gneisses and carbonate rocks in the catchment area (<1 ppm Mo). Similar Mo enrichment is characteristic of all marine euxinic basins (Tribovillard et al., 2006; Lyons et al., 2009; Scott and Lyons, 2012), and Lake Cadagno offers a lacustrine complement where the Mo cycling and burial pathways from waters to sediments have been studied in detail (Dahl et al., 2010a).

2.2. Sampling: the ETH drilling project

Sediment samples were taken in September 2009 as part of the FloodAlp drilling project led by A. Gilli from ETH-Zürich. Our samples come from two sediment cores taken from the deepest part of the lake. One short gravity core (SC) was collected from the uppermost 1 m to ensure undisturbed surface sediments, and one long core (CDP) was collected using an UWITEC platform with a percussion piston-coring system in nine 1-m segments totaling 9 m of recovered sediment. The sediments were deposited during the last 9800 years of the Holocene period, when the lake arguably was stably stratified with anoxic and sulfidic bottom waters (see Supplementary content for details). The drill core contains 'regular' autochthonously produced lacustrine sediments (RS) and event deposits, including detrital flood deposits (FD) and allochthonous mass-movement deposits (MMD) (Table 2, details in the Supplementary content). Regular sediments consist mainly of bacterial remains and generally contain more Mo than both flood and mass movement deposits that were transported from the oxic zone (Wirth et al., 2012). Therefore, we prioritized the Mo-rich samples to place the focus on euxinic processes. The drill cores were brought into the lab at the field station, opened, and subsampled at 10 cm resolution and transferred into 50 ml Falcon tubes. The headspace of each tube was purged with N_2 to minimize oxidation, and the tubes were subsequently frozen with dry ice. When the samples arrived at Harvard University one week later, there was no evidence of oxidation (rust), and samples were thawed in an anaerobic glovebox with 95% N_2 and 5% H_2.

2.3. X-ray absorption fine structure (XAFS) experiments

For Mo speciation analysis, XAFS sample holders were prepared from a 2 mm thick Teflon plate by cutting rounded holes as sample slots. Windows were made from thin, X-ray transparent Lexan™ plastic and sealed with Kapton™ tape. Samples were thawed and subsampled by first mixing the mud with a spatula and then transferring it into each sample slot. To minimize oxidation, samples were handled anaerobically at all times. Samples were dried with Kimwipes and eventually transported in an anaerobic jar (AnaeroPack) to the National Synchrotron Light Source (NSLS) at Brookhaven National Laboratories and to Stanford Synchrotron Radiation Light source (SSRL) at SLAC National Accelerator Laboratory, USA. O_2 diffusion into the sample could only have occurred during the ~3 hours of analysis through the windows, but the presence of other reduced compounds in the samples (e.g., Fe^{2+}, S^{2-}) added reducing power to the sediment and would have significantly slowed down oxidation of the Mo compound(s) in the samples.

X-ray absorption spectroscopy (XAFS) measurements were made at beamlines X11-A and 4-1 at the NSLS and SSRL, respectively. We used the Si(311) and Si(220) double crystal monochromators in conjunction with harmonic rejection mirrors at NSLS and SSRL, respectively. Fluorescent X-rays were measured using a Canberra multi-channel 13 element Ge detector. We detuned the incident beam intensity by ~20% to reject higher-order harmonic frequencies. Some of the spectra analyzed at SSRL were collected with a Zr metal foil to attenuate scattering.

We processed and analyzed all the data using the Athena and Artemis software packages (Ravel and Newville, 2005). Energy calibration was maintained by simultaneous measurements of a Mo(0) foil in transmission mode as an internal standard. The first three peaks in the first derivative spectra of the Mo(0) foil were assigned 20000.0, 20010.5, and 20024.0 eV (Wichard et al., 2009). These assignments set the absolute energy scale for all characteristic spectral features. We collected all spectra with energy and wave number resolution prior to the edge (19600–19960 eV); across the K-edge (19960–20050 eV); and throughout in the EXAFS region at 5 eV, 1 eV, and 0.05 Å^{-1}. At least four spectra per sample were merged to improve signal-to-noise ratio and also to enhance energy resolution (e.g., better than 1 eV across the K-edge). Usable spectra were collected for 2-mm-thick samples with >16 ppm Mo, but more statistically robust results required samples with >120 ppm Mo. There were no signs of beam damage or photo-oxidation between consecutive spectral measurements.

For data interpretation, collected spectra for tetravalent Mo standards ($Mo(IV)O_{2(s)}$ and $Mo(IV)S_{2(s)}$) and hexavalent standards ($Mo(VI)O_{3(s)}$, $Mo(VI)O_4^{2-}_{(l)}$, and $Mo(VI)S_4^{2-}_{(l)}$) were used as reference compounds (Table 1 and S1). All reagents, except MoS_4^{2-} (Strem Inc.), were purchased from Sigma–Aldrich and measured without further processing other than dilution with boron nitride for solid standards. Published data for other Mo references compounds were used (e.g., Mo(V)–cysteine; Wichard et al., 2009) to support our data analysis.

2.3.1. EXAFS

We processed the extended X-ray absorption fine structure (EXAFS) data by subtracting background absorption using a smooth spline fit and averaging the spectra with Athena Software (Ravel and Newville, 2005). The EXAFS equation for energy absorption is expressed as a series of harmonic functions of wavenumber, k, which is directly related to absorption energy by $E = E_0 + hk^2/4\pi m_e$. Here, m_e and h are the mass of the electron and Planck's constant, respectively.

The EXAFS equation is a follows:

$$\chi(k) = \sum i \mathbf{A_0^2 N_i} \cdot |f(k)|/(k\mathbf{R_i^2}) \cdot \exp[-2\mathbf{R_i}/\lambda(k)]$$

$$\cdot \exp[-2k^2\boldsymbol{\sigma_i^2}] \cdot \sin[2kR_i + \varphi_i]. \tag{1}$$

The fitting parameters in the expression for $\chi(k)$ (highlighted in bold) are coordination number ($\mathbf{N_i}$) of each atom of type i; total amplitude of the photon energy ($\mathbf{A_0}$); the distance of the ith atom to the scattering Mo atom ($\mathbf{R_i}$, subsequently referred to as bond length); and its mean-square deviation in R_i, known as the Debye–Waller factor ($\boldsymbol{\sigma_i}$) (Rehr and Albers, 2000). In this fitting process, the zero point of the energy scale, $\mathbf{E_0}$, was allowed to vary. The rest of the parameters are calculated theoretically in Artemis using FEFF8 code for calculations of atomic scattering amplitudes, including the effective scattering amplitude of

Table 1

Interatomic distances (equivalent to bond lengths) in reference compounds analyzed in this study derived from EXAFS modeling using the Artemis Software package (Ravel and Newville, 2005). Published values are shown for comparison, and the R-factor is used as a performance index with lower values representing better model fits (here fitted in R-space with k^3 weighing within the common range 1.4–4 Å, keeping the ligand numbers (n) fixed).

Standard	Mo–O			Mo–S			Mo–Mo			Reference
	n	r (Å)	σ^2	n	r (Å)	σ^2	n	r (Å)	σ^2	This study, R-factor
$Mo^{IV}O_2$										
	4	1.959					2	2.790		Ressler (2000)
	2	2.062					8	3.709		
	6	2.07 ± 0.04	0.019				2	2.65 ± 0.03	0.006	This study, $R = 0.23$
							8	3.82 ± 0.03	0.011	
$Mo^{IV}S_2$										
				6	2.42		6	3.16		Cramer et al. (1984)
				6	2.41 ± 0.01	0.006	6	3.20 ± 0.01	0.008	This study, $R = 0.01$
$Mo^{VI}O_3$										
	1	1.671					2	3.438		Ressler (2000)
	1	1.735					2	3.696		
	2	1.948					2	3.963		
	1	2.251								
	1	2.332								
	2	1.71 ± 0.05	0.003				2	3.34 ± 0.04	0.003	This study, $R = 0.10$
	2	1.97 ± 0.05	0.003				2	3.77 ± 0.05	0.003	
	2	2.28 ± 0.05	0.003				2	4.03 ± 0.06	0.003	
$Mo^{VI}O_4^{(2-)}$										
	4	1.78	0.003							Bostick et al. (2003)
	4	1.78 ± 0.01	0.003							This study, $R = 0.02$
$Mo^{VI}S_4^{(2-)}$										
				4	2.20	0.005				Bostick et al. (2003)
				4	2.18 ± 0.01	0.005				This study, $R = 0.03$

the backscattering X-ray photons $|f(k)|$, which depends on type and number of neighboring atoms, the effective scattering phase functions φ, and the mean free path, $\lambda(k)$.

First shell fits were established using Mo–S and Mo–O single scattering paths with phase and amplitude functions calibrated against reference materials for which the coordination environment has been described previously as Mo(IV)O$_2$ (Ressler, 2002), Mo(VI)O$_3$ (Ressler, 2000, 2002), Mo(IV)S$_2$ (Dickinson and Pauling, 1923), Mo(VI)O$_4^{2-}$, and Mo(VI)S$_4^{2-}$ (Lapasset et al., 1976). Acceptable model fits satisfied three criteria. First, the global amplitude term, A$_0$, was allowed to float between 0.7 and 1.1 but was fixed at the same value for all individual shells. Second, Debye–Waller terms, σ_i^2, were allowed to float but were constrained within a range of 0.003–0.020 Å^2 for all shells, consistent with model compound fits. Third, the energy shift was no bigger than $|E_0| < 10$ eV. Also, the bond length was allowed to vary, but model parameters were iteratively recalculated if the estimated distance to the excited Mo atom greatly exceeded the initial guess (or known value in the case of our reference materials): $\Delta R = |R - R_{\text{expected}}| < 0.5$ Å. The best model fit was chosen among acceptable fits based on the model run with lowest R-factor (best goodness of fit), and third shell atoms were only added if they improved the goodness of fit. To discard other possibilities, scattering from other atoms was fitted using Mo–O, Mo–S, Mo–Mo, Mo–Fe, and Mo–C scattering paths (see Table S2 in Supplementary con-

tent). Finally, the contributions of multiple scattering paths were evaluated (for SC3-X and CDP70-X), but did not contribute significantly to the spectra and therefore were omitted in the final fits (see Table S3 for details in the Supplementary content).

The fitting procedure was performed step-wise with simple models applied first, one atomic shell at a time. Our results show that the model fits did well at reproducing known bond lengths (R_i), type of atom, and coordination number (N_i) (Table 1). We used the goodness of fits obtained for known reference materials to guide our choice of preferred models. The $\chi(k)$ function was Fourier transformed using k^3 weighting to perform model fits both on the raw absorption spectrum (k-space) and on Fourier transformed data (R-space). The fitting domain was chosen to the maximal range ($k = 3$–9 Å^{-1}; $R = 1.4$–4 Å), that is, where all spectra were well defined to ensure that the performance index (R-factor) could be compared. Applying both fitting procedures to our reference materials and keeping the number of ligands fixed at known values, our shell-by-shell modeling procedure accurately determines atomic distances for first and second neighboring atoms (O and S) and gives slightly offset results (<0.10 Å) for third shell Mo–Mo distance in MoO$_2$ or MoO$_3$. Both fitting procedures yielded consistent results, but R-space fitting yielded better performance index (i.e., $R_R < R_k$) and gave more precise atomic distances. The goodness of fit (in R-space) for reference materials is better than $R_R < 0.23$ Table 1. There-

Table 2
Fitting results for euxinic sediment samples: interatomic distances (e.g. bond lengths) in anoxic sediment samples were obtained using a hypothetical three shells model with Mo–O, Mo–S and Mo–Fe bonds. Multiple scattering paths did not improve the fits and have been ignored. All model fits, except the most dilute sample (CDP20-X, 16 ppm Mo), yield better goodness of fit than obtained using the same for reference materials (Table 1) using the shell-by-shell fitting approach in R-space. The models yield consistent results when fitted in k-space, although several samples (marked with an asterisk) yield a lower or comparable goodness of fit (R_k) than reference materials. Structures with three of less Mo ligands have been ignored.

Sample	Depth[1] (cm)	Age[2] (yr)	[Mo] (ppm)	Group	Mo–O			Mo–S			Mo–Fe			Goodness
					n	r (Å)	σ^2	n	r (Å)	σ^2	n	r (Å)	σ^2	R_R-factor
SC1_X	0–3	0	179	Type S				4	2.26 ± 0.02	0.010	1	2.72 ± 0.03	0.003	0.14*
SC3_X	7–11	35	155	Type S				4	2.32 ± 0.03	0.013	1	2.72 ± 0.03	0.003	0.04
SC5_X	15–19	143	120	Type OS	2	1.73 ± 0.03	0.003	2	2.31 ± 0.04	0.003	1	2.73 ± 0.06	0.003	0.09
CDP6_X	93–103	726	190	Type OS	2	1.73 ± 0.03	0.006	2	2.36 ± 0.03	0.003	1	2.77 ± 0.04	0.003	0.08
CDP9_X	124–134	1173	88	Type S				4	2.24 ± 0.06	0.006	1	2.71 ± 0.12	0.003	0.24*
CDP20_X	236–246	2005	16	Type OS	1	1.69 ± 0.17	0.003	3	2.29 ± 0.09	0.006				0.29*
CDP30_X	365–375	3374	38	Type OS	2	1.74 ± 0.03	0.005	2	2.36 ± 0.03	0.005				0.17*
CDP70_X	782–792	6875	197	Type S				4	2.33 ± 0.03	0.007	1	2.73 ± 0.05	0.003	0.03
CDP80_X	884–894	9279	140	Type S				4	2.38 ± 0.03	0.008				0.13*

[1] Sample depths represent 4 cm and 10 cm stratigraphic intervals in the short core (SC) and long core (CDP), respectively.
[2] Ages were determined from eight evenly distributed ^{14}C dated levels in the drill core and interpolated using an age-model that compensates for turbiditic mass-movements (Wirth et al., in preparation).

fore, we adopt this threshold as quality control to determine which models were accepted for our samples.

For example, MoS_4^{2-} was accurately fitted to a model with four S atoms in one shell at 2.18 ± 0.01 Å atomic distance, yielding an R-factor of 0.03 (goodness of fit), which is indistinguishable from previous EXAFS analysis at 2.20 ± 0.03 Å (Bostick et al., 2003). These EXAFS results also fit bond lengths obtained using crystallographic techniques with four sulfur atoms sitting at 2.171 ± 0.005 (n = 1), 2.177 ± 0.005 (n = 2), and 2.186 ± 0.006 Å (n = 1) (Lapasset et al., 1976). The same procedure was successfully applied for Mo–O bonds in MoO_2 to yield precise (but less accurate, ±0.10 Å) Mo–Mo atomic distances manifested with a lower goodness of fit, R-factor = 0.23. Even greater offsets in atomic distance often failed to fit the spectra and always gave significantly worse R-factors. For example, a one-shell model cannot fit the five distinct Mo–O shells in MoO_3 at atomic distances ranging from 1.67 to 2.33 Å, and our step-wise approach yielded acceptable fits only when three Mo shells were included in the model. Therefore, we used the R-factor as a statistical measure to determine when a model successfully identifies the type of neighboring atoms and the inter-atomic distances at the level of accuracy defined by our reference materials. Our interpretation of the Mo molecular structure in the lacustrine mud samples is therefore founded on models with R-factors better than those obtained for the reference materials.

2.3.2. XANES

Signal analysis of the XANES spectra was performed in MatLab®. A cubic smoothing spline, $\chi(E)$, was fitted to the data and used to determined the first and second derivative spectra. This approach allowed us to smooth the noise and define a rigorous procedure for the identification of peaks and inflection points in the XANES spectra. The smoothing function contains one free parameter, ρ, which determines the relative weight placed on the contradictory demands of having spectra χ smooth ($\rho = 0$) vs. having χ close to

the data ($\rho = 1$). For values of ρ between 0.2 and 0.9, the derived oxidation states were similar for all samples, except in two cases with relatively low Mo concentrations (Mo = 16–38 ppm).

The reference materials show consistent correlations between oxidation state and K-edge, with higher E_K for higher oxidation states (edges are defined in the caption of Fig. 4). Further, there is a systematic shift in maximum peak position (E_M), with greater energy difference for Mo–S compounds than for Mo–O. This relationship is explored further in Section 3.2, and it shows how E_K and E_M in the XANES region can be used to determine ligand type and to select the correct calibration curve for determinations of the oxidation state.

An oxidation test of the samples was performed to confirm the presence of initially reduced Mo compounds in our samples. If Mo is present at a low oxidation state (IV or V), then oxidation should result in a positive shift of the K-edge in the XANES spectrum (Table 3). A few samples were chosen for this analysis and oxidized in either one or two steps. As a first oxidation step, anoxic sediments (e.g., sample CDP9-X) were exposed to air and dried in an oven at 70 °C over night (defined as CDP9-Y). In the second step, the samples were ashed at 700 °C to combust organic matter in an O_2-rich atmosphere (renamed as CDP9-Z).

Linear combination fitting was applied to determine the Mo species and quantities of known materials in the (perhaps heterogeneous) samples. However, this approach is feasible only if XAFS spectra of the constituent(s) in the sample exist in our database. Therefore, each observed spectra were fitted separately to a linear combination of known end-member spectra in XANES region (formulated in terms of derivative XANES spectra defined at −30 to 150 eV around the K-edge) and the EXAFS region (EXAFS spectra in the k-range from 3 to 9 Å^{-1}). If the two fits did not converge on the same quantities of end-member constituents in the two spectral regions (within a few%), then at least one additional (unknown) Mo-compound must be present in the sample, and we rejected the estimated propor-

Table 3
XANES peaks identified using Matlab. The spectra were smoothed using a cubic spline fit with one free parameter (ρ) that determines the relative importance of having the curve smooth ($\rho \rightarrow 0$) vs. having the curve close to observed data ($\rho = 1$). The peaks are determined where the first derivative equals zero. Edges are defined at the steepest ascend and were determined at the maximum peaks of the first derivative spectrum.

Sample	ρ Smoothing factor	Pre-edge Inflection	Pre-peak Peak	E_K (eV)	E_M (eV)	E_M–E_K (eV)
Reference materials						
Mo-foil				0.0	16.0	16.0
Mo(V)-cys (Wichard et al., 2009)		5.0		15.0	36.0	21.0
MoO_2	0.2	–	–	11.9	24.0	12.1
MoO_3	0.8	2.7	6.1	14.4	26.2	11.9
MoO_4^{2-} (liquid)	0.8	2.7	5.2	16.8	42.7	25.9
MoS_4^{2-} (liquid)	0.5	1.3	–	10.1	45.5	35.4
MoS_2	0.8	–	–	6.1	30.1	24.0
Anoxic Type S						
SC1-X	0.5	–	–	7.0	34.8	27.8
SC3-X	0.5	–	–	6.3	30.9	24.5
CDP9-X	0.5	–	–	7.6	31.7	24.0
CDP70-X	0.5	–	–	6.6	31.4	24.8
CDP80-X	0.5	–	–	6.6	34.1	27.6
Anoxic Type OS						
CDP20-X	0.2	3.7	–	6.1	36.0	29.9
SC5-X	0.50	1.8	–	16.9	36.5	19.6
CDP6-X	0.40	1.1	–	15.3	36.2	20.9
CDP30-X	0.2	1.7	–	9.8	33.8	24.0
Oxidized						
SC5-Z	0.5	1.5	4.8	15.7	39.4	23.7
CDP6-Y	0.5	2.3	7.6	15.7	37.3	21.6
CDP9-Y	0.5	0.9	4.7	15.3	42.2	26.9
CDP9-Z	0.5	1.9	6.8	15.4	46.6	31.2
CDP30-Z	0.5	1.1	4.3	15.6	41.9	26.4
CDP80-Z	0.5	1.3	4.9	15.2	40.5	25.3

tions. Conversely, if a sample spectrum can be written in terms of the same linear combination (same quantities) of known spectra from our database in the two distinct parts of the XAFS spectrum, then we assumed the sample contains the given Mo compounds.

3. RESULTS

3.1. Mo EXAFS of the euxinic sediments

The EXAFS spectra of our samples show two distinct spectral types (Fig. 3). These two spectra are easily identified from the Fourier transforms of the EXAFS spectra where either a dominant mode is found for "Type S" or two dominant modes are observed for "Type OS". EXAFS model fits show that these modes reflect Mo compounds with either (1) exclusively Mo–S bonds or (2) a mixture of Mo–O and Mo–S bonds in Type S and Type OS, respectively.

In both spectral types, the Mo–S bond lengths range from 2.24 to 2.38 Å (Table 2). This range is significantly longer than the bond length for hexavalent $Mo(VI)S_4^{2-}$ (2.18 ± 0.01 Å) and shorter than for tetravalent $Mo(IV)S_2$ (2.41 ± 0.01 Å); note that higher atomic charge pulls the neighboring atoms closer. In contrast, the Mo–O bonds in Type OS sediments are found at 1.69–1.74 Å, which

are distinctly shorter than the Mo–O bonds in tetravalent $Mo(IV)O_2$ at 2.0 Å but compare well with terminal Mo=O in hexavalent compounds $Mo(VI)O_4^{2-}$ and $Mo(VI)O_3$ at 1.78 and 1.75 Å (Table S1), respectively. From this, we conclude that both types of samples contain bridging Mo–S ligands, and there are terminal Mo=O bonds in Type OS samples (Table S1, Fig. 7).

Under ideal circumstances, the XAFS technique can provide information about atoms well beyond the first Mo–S shell. The fitting results are marginally improved by adding either Mo or Fe in the second or third shell at 2.99–3.00 Å (Table S2) and 2.71–2.77 Å, respectively. The presence of Mo in the third shell is rejected because the predicted Mo–Mo distance is unrealistically long when compared to known Mo dimer compounds bridged through S at 2.72–2.94 Å (Table S1). The obtained Mo–S and Mo–Fe interatomic distances are most similar to those for MoFe proteins Avl and Cpl in nitrogen fixing bacteria *Azotobacter vinelandii* and *Clostridium pasteurianum* measured with EXAFS at 2.35–2.39 and 2.69–2.70 Å, respectively (Cramer et al., 1978; Chen et al., 1993). Given the limited number of Mo–S compounds in the EXAFS database (Table S1), this comparison is probably more illustrative than definitive; for example, the chemical properties of the Mo–S compounds in natural euxinic environments are entirely unexplored.
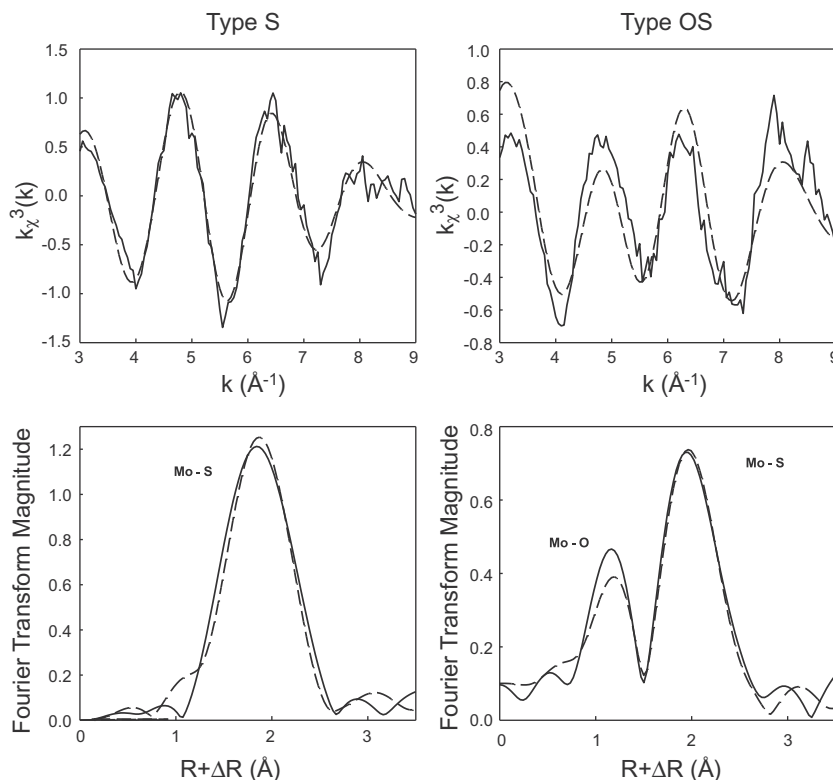
Fig. 3. EXAFS spectra of the two spectral types with k-representation in upper panels and the Fourier transform shown in the lower panels. Type S and Type OS spectra are represented by CDP70-X and CDP6-X in the left and right panels, respectively. Solid line: data, dashed line: model.

Five of our nine samples display a Type S spectrum and reveal that Mo is exclusively coordinated to four sulfur atoms (Table 2). In Type OS samples, Mo is coordinated to one or two oxygen atoms and two or three sulfur atoms. The Mo–S compounds are found both in the most recent sediments in Cadagno at <0.3 m depth in core and in the early Holocene (deepest) samples from 7 to 9 m depth (∼9 kyrs old). All Type S samples are extremely enriched in Mo (>120 ppm, see Table 2), and two Type OS samples are highly enriched (120–190 ppm), while two samples with 'Type OS-like' spectra display much lower Mo concentrations (16–38 ppm).

3.2. Mo XANES of the euxinic sediments

The XANES region of the spectrum contains unique information about the oxidation state. The mean Mo oxidation state in a natural sample was derived from the Mo K-edge position (E_K) by comparison to the linear correlation observed for reference materials. Specifically, there are excellent linear relationships between E_K and Mo oxidation state. Reference compounds are used to generate a calibration curve from which oxidation states of the samples are calculated (see statistics in the caption of Table 4).

The position of the K-edge (Fig. 4) also depends on the electronegativity of the ligands, so that higher E_K values are seen for the Mo–O compounds compared to the Mo–S compounds. Fortunately, Mo–O and Mo–S bonding environments can be distinguished from the EXAFS spectrum

to optimize the choice of calibration curve. Here, we further suggest that standard-reference matching can be performed using the XANES spectrum alone (i.e., independent of EX-AFS) and propose that the position of the maximum peak (E_M) in the post-edge region is a diagnostic feature for distinguishing Mo–O from Mo–S coordination environments (Fig. 5).

Together, the two spectral features in the XANES region, E_K and E_M, allow for an operational distinction of ligand type (Table 3), since Mo–S compounds display a much larger maximum peak displacement (E_M–E_K) than do Mo–O compounds (Fig. 5). The shorter Mo–O bonds (1.7–2.0 Å) fall on a linear trend at higher E_K and with a distinctly smaller energy difference from edge to maximum absorption compared to Mo–S compounds, which have longer bond lengths (2.2–2.4 Å). The maximum absorbance peak falls in the part of the XANES spectrum associated with multiple scattering resonances, so that E_M position is interpreted to reflect the immediate coordination environment. The correlation in Fig. 5 is observed for both reference materials, for which the molecular structure is known, and for natural samples where the coordination environment is determined from the EXAFS spectrum.

Fig. 5 shows that Mo compounds with higher atomic charge (oxidation state) display higher E_K (and energy shift [$E_M - E_K$]). The Mo(IV)–S and Mo(VI)–S reference compounds display K-edges at 20006.1 and 20010.1 eV, respectively. The Mo(IV)–O, Mo(V)–O, and Mo(VI)–O reference compounds have K-edges at 20011.9, 20015.0, and

Table 4
Oxidation state estimates for anoxic sediment and after an oxidation treatment. The mean oxidation state is obtained in two ways from two distinct calibration curves. We use the EXAFS result to determine whether Mo–O or Mo–S calibration curve is applicable. The calibration curves for Mo–O and Mo–S compounds were based on $Mo^{VI}O_4^{2-}$, Mo^V-cysteine, $Mo^{IV}O_2$ and $Mo^{IV}S_2$, $Mo^{VI}S_4^{2-}$, respectively. Oxidation states (q) estimates were obtained from the E_K spectral feature while E_M feature was used as a quality-check to assure that we are matching standards with similar coordination geometry. We applied linear relationships $q_i = aE_i + b$ with Pearson correlation coefficient, R, and observed a consistent slope for both the Mo–O and Mo–S array. For E_K the calibration curve (a, b, R) was given by (0.42, −1.06, 0.98) and (0.40, −1.77, 1.00) for Mo–O and Mo–S, respectively. For E_M the calibration curve was given by (0.10, 1.52, 0.99) and (0.13, 0.16, 1.00), respectively. Bold values do not meet quality criteria.

Sample	Spectral type	Treatment	Depth (cm)	Age (yr)	[Mo] (ppm)	Calibration array	Smoothing	Average Mo oxidation state		
							r	Using E_M	Using E_K	Mean + 1sd
SC1_X	S	Anoxic	−1	0	179	Mo–S	0.5	4.6	4.5	4.5 ± 0.1
SC3_X	S	Anoxic	15	35	155	Mo–S	0.5	4.1	4.1	4.1 ± 0.0
SC5_X	OS	Anoxic	35	143	120	Mo–O	0.5	5.2	5.8	5.5 ± 0.4
CDP6_X	OS	Anoxic	93	726	190	Mo–O	0.4	5.2	5.4	5.3 ± 0.1
CDP9_X	S	Anoxic	124	1173	88	Mo–S	0.5	4.2	4.8	4.5 ± 0.4
CDP20_X	OS	Anoxic	236	2005	16	Mo–O	0.2	5.2	2.7	**3.9 ± 1.8**
CDP30_X	OS	Anoxic	365	3374	38	Mo–O	0.5	4.9	3.0	**4.0 ± 1.4**
CDP70_X	S	Anoxic	782	6875	197	Mo–S	0.5	4.2	4.3	4.2 ± 0.1
CDP80_X	S	Anoxic	884	9279	140	Mo–S	0.5	4.5	4.2	4.4 ± 0.2
Oxidized samples										
SC5-Z	was OS	O_2 + 700 °C	15		120	Mo–O	0.5	5.5	5.5	5.5 ± 0.0
CDP6-Y	was OS	O_2 + 70 °C	93		190	Mo–O	0.5	5.3	5.5	5.4 ± 0.1
CDP9-Y	was S	O_2 + 70 °C	124		88	Mo–O	0.5	5.8	5.4	5.6 ± 0.3
CDP9-Z	was S	O_2 + 700 °C	124		88	Mo–O	0.5	5.5	5.4	5.4 ± 0.1
CDP30-Z	was OS	O_2 + 700 °C	365		38	Mo–O	0.5	5.8	5.4	5.6 ± 0.2
CDP80-Z	was S	O_2 + 700 °C	884		140	Mo–O	0.5	5.7	5.3	5.5 ± 0.2

20016.8 eV, respectively. The highly distorted octahedral lattice of MoO_3 falls outside the array given by the rest of the Mo–O compounds and might constitute a separate Mo–O array with MoO_2 (Ressler, 2000). Likely, the energy shift depends on the multiple scattering resonances and the geometry of the compounds. Nevertheless, the two spectral features provide a fingerprint that readily distinguishes Mo–O from Mo–S bonding environments. This XANES fingerprint is used to confirm that the Mo oxidation state is determined using the calibration curve (E_K vs. oxidation state) established from compounds with similar coordination environment (Table 4).

The mean Mo oxidation state of our samples falls in two distinct groups that coincide with each EXAFS spectral type. Type S (Mo–S) samples range from 4.1 to 4.5, whereas Type OS compounds with high Mo content (SC5-X and CDP6-X) display a significantly higher mean oxidation state at 5.3-5.5 (Table 4). All Type S compounds have a calculated mean oxidation state of 4.3 within ±0.2 units (1 standard deviation of the mean; see caption of Table 4). Two Type OS samples with low Mo concentration (CDP20-X and CDP30-X) contain EXAFS spectral features that indicate oxygen in the first shell and yet fall outside the Mo–O array of oxidation states. These two samples also show spectra that fall considerably off the linear trend between E_M and E_K defined by the other samples. This offset would be expected for samples with different coordination chemistry and artificial features associated with low signal/noise ratio (Fig. 4). Hence, we can use the E_M vs. E_K characterization in Fig. 5 as a quality control and

choose calibration standards with similar geometry for a reliable determination of oxidation state.

None of the Type S samples display a pre-peak or a pre-edge inflection. This characteristic is shared with known tetravalent Mo compounds ($Mo(IV)O_2$ and $Mo(IV)S_2$) and is thus a similarity between Type S compound(s) and molybdenite. However, Type S compounds are otherwise distinct from tetravalent MoS_2 in the edge and post-edge regions of the XANES spectra, in that E_K and E_M are at distinctly higher energies and, thus, the average Mo oxidation state in the samples is slightly higher than four. Type OS compounds display a pre-edge inflection but not a genuine pre-peak. Distinct pre-edge inflections in the XANES region are observed in compounds with higher Mo oxidation states at +6 and +5 ($Mo(VI)S_4^{2-}$, $Mo(VI)O_4^{2-}$, and $Mo(VI)O_3$; e.g., this study and Mo(V)–cysteine and Mo(V)–azotochelin (Wichard et al., 2009), while strong pre-peaks are associated with Mo=O (e.g., $Mo(VI)O_4^{2-}$)).

3.3. Oxidation experiments with reduced Mo compounds

Oxidation experiments were performed to confirm the presence of reduced Mo in both types of samples. As sediment samples were exposed to the oxic atmosphere and left in an oven overnight at 70 °C, both E_K and E_M were dramatically shifted to higher values. Oxidized Mo–S samples plot within the Mo–O array in Fig. 5, and their EXAFS spectra confirm that most sulfur bonds have been broken and replaced with Mo–O ligands (Table 5, discussed further below). Oxidized sediments display significantly higher oxi-
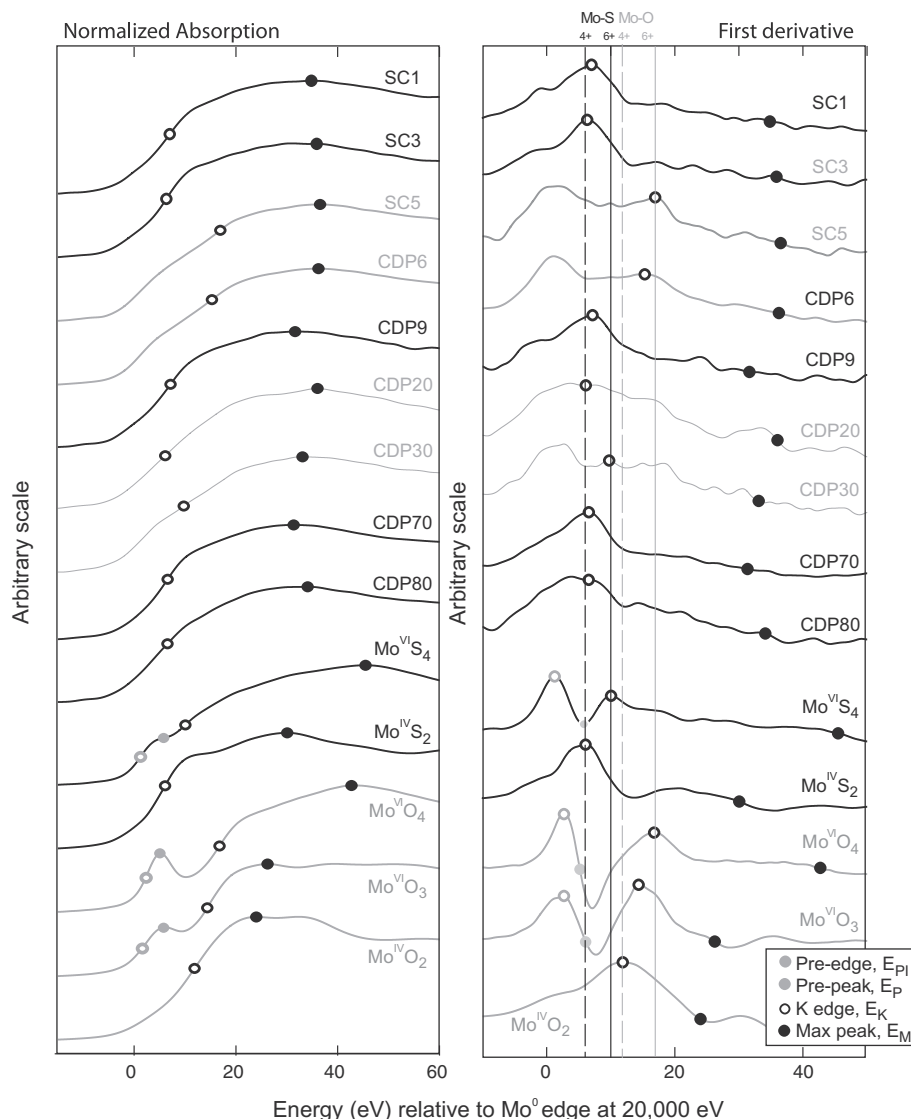
Fig. 4. XANES spectra (left panel) and derivative spectra (right panel) of sediment samples and reference compounds. We determined edges and peaks using a MatLab algorithm (Supplementary information). The position of the K-edge, E_K, is defined at the steepest ascent on the main absorption edge, (max $\chi'(E)$ and $\chi''(E) = 0$). The maximum peak, $E_M > E_K$ is defined at energies with maximum absorption, (max $\chi(E)$ and $\chi'(E_M) = 0$), which is also the first absorption peak above the K-edge for samples with good signal to noise ratio. If present, a pre-edge and pre-peak were defined by the same mathematical criteria at energies below the main edge. Spectral features are summarized in Table 3 and always appear in the following order $E_{PI} < E_P < E_K < E_M$ with E_P within 20004–20010 eV, E_K within 20005–20017 eV, and E_M within 20014–20046 eV for Mo–O and Mo–S compounds studied here.

dation state estimates with little variation among samples, at 5.5 ± 0.1, both for ex-Type S and ex-Type OS samples (Table 4). Even the two samples with low Mo content, once oxidized, fall in the Mo–O array in Fig. 5. Upon ashing and further oxidation, the edge positions did not move any further. Hence, there is no evidence of further oxidation upon combustion at 700 °C.

Upon oxidation, both Type S and Type OS sediments developed the 'oxo-edge' (pre-edge) features characteristic of terminal Mo=O bonds. More pronounced pre-peaks were seen after the samples were ashed at 700 °C (Fig. 6). Mo–O bond lengths in oxidized samples (Table 5) at 1.74–1.78 Å compare well with the double bonds in hexava-

lent molybdate at 1.78 Å, and they are distinctly shorter than both tetravalent Mo(IV)O$_2$ at 2.0 Å and pentavalent single bonded Mo–cysteine at 1.93 Å (Knox and Prout, 1969) (Fig. 7; Table S1). The ashed samples display more pronounced pre-peaks in the XANES spectrum compared to the oxidized dry samples, suggesting more terminal Mo=O bonds in the ashed samples.

3.4. Linear component analysis

The observed sensitivity to air (oxidation) raises the concern of whether or not our samples could have suffered from oxidation during sampling, handling, or analysis. To
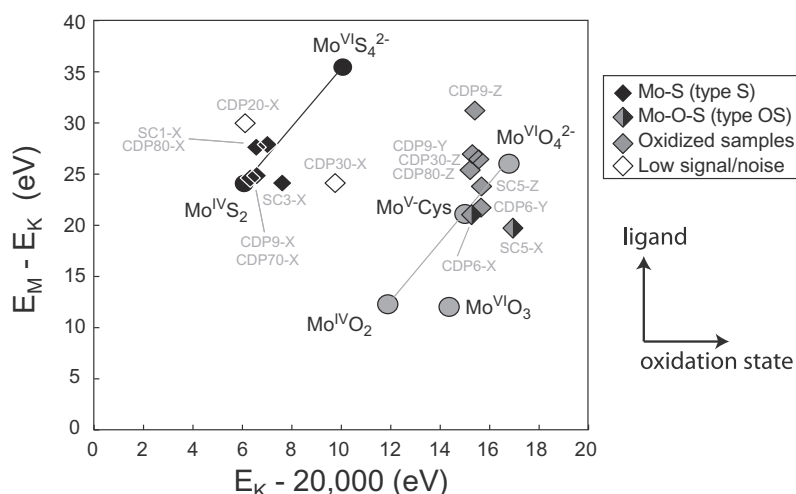
Fig. 5. XANES spectral characteristics plotted as E_M–E_K vs. E_K reveal a simple operational distinction between Mo–O vs. Mo–S bonding environments and oxidation state. Color codes refer to the ligand type determined from EXAFS, and all oxidized samples are coordinated to oxygen. Note that the two variables are linearly dependent and therefore E_M–E_K would plot on a trend line with negative slope as function of E_K, for random data with greater variance of E_K than for E_M. The positive correlations are not random scatter, but results from a true spectral difference between Mo–O and Mo–S compounds, where sulfur ligands with generally longer bond lengths plot with lower E_K (lower electronegativity) and higher E_M–E_K than Mo–O compounds.

Table 5
Simple two or three shells EXAFS model fits to euxinic mud samples subject to heating and oxidation. Interatomic distances (e.g. bond lengths) in the sediment samples were obtained using a hypothetical one, two or three shells model with Mo–O, Mo–S, and Mo–Fe bonds. Further details in Table 2. The models yield consistent results when fitted in k-space, although CDP9-Y (*) yields a lower or comparable goodness of fit (R_k) than our model fits to the reference materials (marked).

Sample	Treatment (cm)	Depth (cm)	Type prior to treatment	[Mo] (ppm)	Mo–O			Mo–S			Mo–Fe		R-factor
					n r (Å)	σ^2		n r (Å)	σ^2		n r (Å)	σ^2	
SC5_Z	700 °C	15–19	OS	120	4 1.77 ± 0.01	0.003					1 2.94 ± 0.02	0.003	0.17
CDP6_Y	70 °C	93–103	OS	190	3 1.77 ± 0.02	0.006		1 2.39 ± 0.04	0.003		1 2.92 ± 0.04	0.003	0.07
CDP6_Z	700 °C	93–103	OS	190	4 1.77 ± 0.04	0.003					1 2.95 ± 0.07	0.006	0.13
CDP9_Y	70 °C	124–134	S	88	3 1.74 ± 0.04	0.003		1 2.37 ± 0.07	0.008		1 2.96 ± 0.19	0.019	0.17*
CDP9_Z	700 °C	124–134	S	88	4 1.77 ± 0.06	0.003					1 2.85 ± 0.05	0.003	0.27
CDP30_Z	700 °C	365–375	OS	38	4 1.77 ± 0.03	0.003					1 2.91 ± 0.05	0.003	0.19
CDP80_Z	700 °C	884–894	S	140	4 1.78 ± 0.04	0.003							0.18

test this possibility, Type OS spectra were compared to the oxidized Type S spectra. Type OS spectra show a nice linear combination of the anoxic Type S (CDP9-X) spectrum and the oxidized Type S spectrum (CDP9-Y) in roughly equal proportions (Table 6), whereas Type S spectra contain only 15–20% of the oxidized Mo species. This could reflect different degrees of partial oxidation. The same proportions were found when fitting the XANES and EXAFS regions separately (Table 6). Hence, Type OS spectra match the expected spectra of a partially oxidized Type S sample. This pattern may reflect either Mo oxidation after the drill core was recovered (e.g., at the beamline) or formation of a Type OS (Mo–O–S) compound in the lake via a novel chemical pathway.

By linear combination fitting, we tested whether any of the reference materials were principal components of the samples. For Type S samples, only $Mo(IV)S_2$ is a likely candidate; tetrathiomolybdate does not constitute a significant component in the observed spectra, since the two spectral regions give inconsistent fitting results (Table 6). To explore post-depositional molybdenite formation further, we also fitted the deeper sediment samples to linear combinations of the MoS_2 reference and the sample from the sediment-water interface (SC1-X). Again, the two spectral regions give inconsistent results (Table 6), which tells us that either MoS_2 or the Mo compound(s) in SC1-X are not principal components in samples from greater depth, – or that neither is important. In any case, the natural samples contain an additional major Mo component distinct from MoS_2.

4. DISCUSSION

4.1. Mo oxidation state and coordination environment

Our XAFS analysis at the Mo K-edge elucidates the molecular structure around Mo in euxinic sediments from Lake Cadagno. Our results suggest that we have discovered a reduced Mo–S species distinct from previous studies in
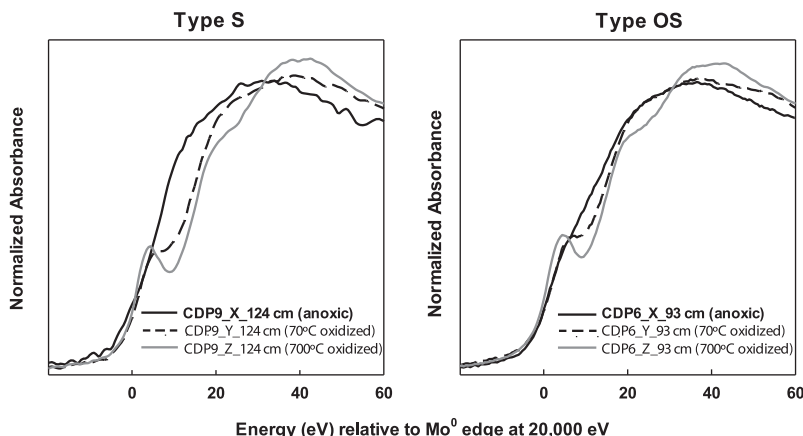
Fig. 6. XANES spectra of oxidation experiments for the two types of Mo-spectra found in Lake Cadagno. Left panel: Mo is exclusively coordinated to S atoms (Type S, CDP9). Right panel: Mo is coordinated to O and S atoms (Type OS, CDP6). Spectra for anoxic samples (X, solid line), oxidized at 70 °C (Y, dashed line) and oxidized at 700 °C (Z, grey line). Oxidation of the anoxic sample alters the position of the pre-edge, K-edge, and the first peak in the multiple scattering resonance part of the spectrum.
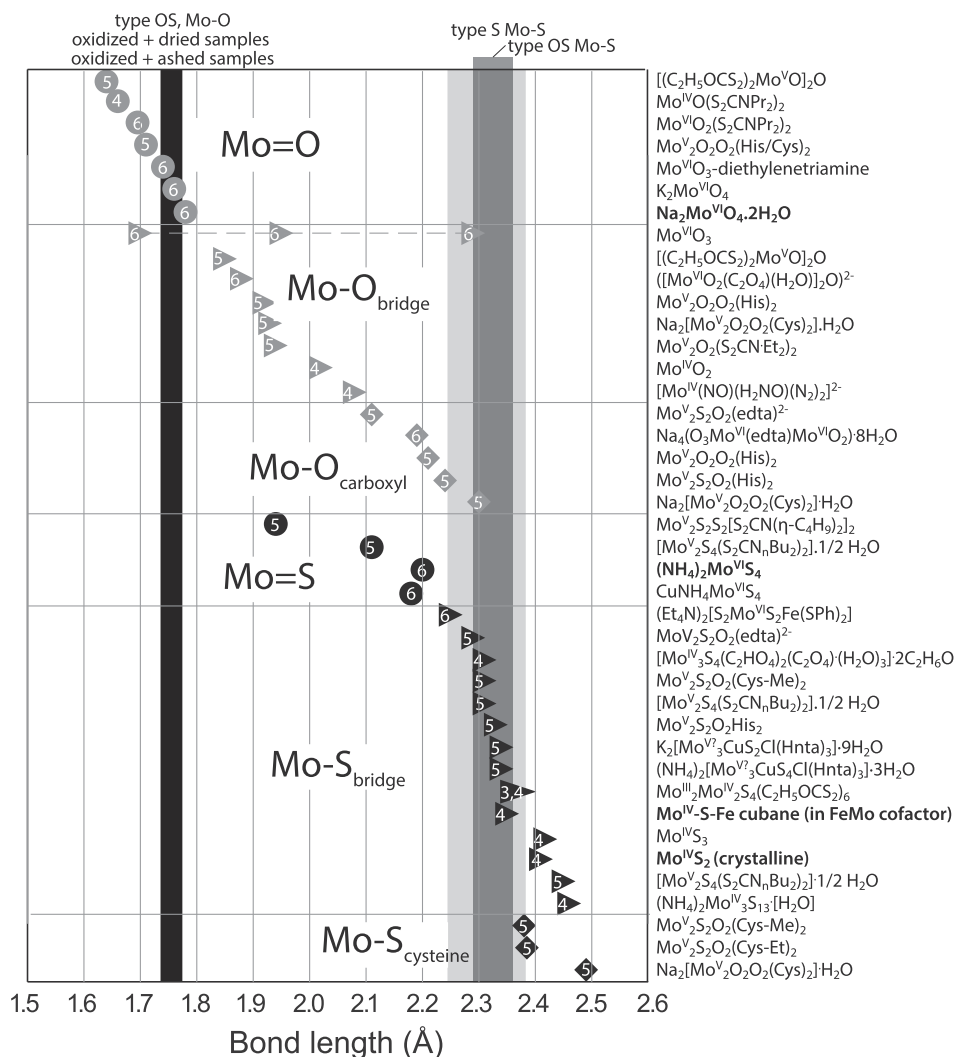

Fig. 7. Bond lengths in selected Mo(IV), Mo(V) and Mo(VI) compounds. Double bonds are significantly shorter than single bonds, and oxygen bonds are significantly shorter than sulfur bonds. The oxidation state (white numbers) is not the only factor controlling bond length, but there is a trend with longer bonds for lower atomic charge. References are summarized in the supplementary information.

Table 6

Linear combination fitting results showing the proportion of oxidized type S Mo-compounds in type OS samples and the proportion of additional MoS_2 at depth relative to the sample at the sediment–water interface. Results are compared for fitting XANES derivative, deriv(E), and EXAFS regions, chi(k), separately to provide a validity check. The weights positive values forced to sum 1. Invalid linear combinations are marked with bold representing fits that either fail completely or give distinct results in the two spectral regions (n.a. = not assessed with Artemis).

Sample	Spectral type	Depth (cm)	Mo (ppm)	XANES derivative −30 eV to +150 eV (%)	EXAFS 3.0–9.0 Å^{-1} (%)
Proportion of oxidized type 1, CDP9-Y (with complimentary CDP9-X)					
CDP6-X	Type OS	15–19	190	60 ± 4	65 ± 3
SC5-X	Type OS	35–39	120	58 ± 3	66 ± 4
CDP20-X	Type OS	236	16	44 ± 6	48 ± 6
CDP30-X	Type OS	365	38	58 ± 4	63 ± 4
SC3-X	Type S	15–19	155	17 ± 4	19 ± 4
CDP70-X	Type S	782–792	197	15 ± 4	20 ± 4
CDP80-X	Type S	884–894	140	**32 ± 4**	**42 ± 5**
Proportion of molybdenite, MoS$_2$ (with complimentary SC1-X)					
SC3-X	Type S	15–19	155	**37 ± 5**	**20 ± n.a.**
SC5-X	Type OS	35	120	**Does not fit**	**32**
CDP6-X	Type OS	93	190	**Does not fit**	**29**
CDP9-X	Type S	124	88	**29 ± 8**	**2 ± n.a.**
CDP20-X	Type OS	236	16	**Does not fit**	**11 ± n.a.**
CDP30-X	Type OS	365	38	**Does not fit**	**31 ± n.a.**
CDP70-X	Type S	782-792	197	**49 ± 5**	**36 ± n.a.**
CDP80-X	Type S	884-894	140	**22 ± 6**	**35 ± n.a.**

ancient black shales. The average Mo oxidation state within sediments (Type S) is estimated at 4.3 ± 0.2 (1 SD, precision), and Mo is exclusively coordinated to S at bond lengths of 2.24–2.38 Å. A few sediment samples do display spectra (Type OS) with a distinctly higher oxidation state (estimated at 5.5 ± 0.1) and the presence of both Mo–O and Mo–S ligands. These Type OS spectra compare well with previous data for black shales, suggesting that they share the same formation history (discussed further below).

Our oxidation experiments confirm that Mo is reduced in the (Type S) euxinic sediments and that the few sediment samples showing higher oxidation states (Type OS) experienced oxidation and related oxygen substitution either during or after deposition. Mo oxidation occurred in Type S samples left to dry at 70 °C in an O_2-rich atmosphere for $\sim$12 h. In contrast, oxidized Type OS Mo compound(s) were not further oxidized by this treatment. Specifically, after combustion in air, there was no further increase in oxidation state. This relationship is best explained if Mo was already present in its fully oxidized +6 state. This interpretation implies that our estimate for average oxidation state, 5.5 ± 0.1, is systematically underestimated by up to 0.5 units. We propose that this discrepancy is best explained by mismatching of the Mo–O compounds to reference materials (here $Mo^{VI}O_4^{2-}$) with different coordination geometry or oxidation state of the ligand, which may slightly offset K-edge position (e.g., 1 eV). Similarly, the oxidation state estimate for Mo–S compounds depends on how well the structure and oxidation state of the ligands in MoS_2 are representative of the Mo coordination geometry in our samples. With this uncertainty in mind, it is possible that all Mo in Type S compounds is in the 4+ state. In the absence of any Mo(V)-S reference compound in our

database, it is impossible to quantify the proportion of Mo(V) in our samples. Nevertheless, we can conclude that our Type S samples contain predominantly Mo(IV)–S compounds and that these compounds oxidize to Mo(VI)–O phases upon exposure to air.

4.2. Desiccation and air sensitivity of the euxinic Mo(IV)–S compounds

The air-sensitivity of the Mo–S compounds in Lake Cadagno is a distinguishing characteristic of the natural euxinic Mo compound(s). Type OS spectra resemble oxidized Mo with both oxygen and sulfur ligands that can be explained if first deposited as Type S compounds (Mo(IV)–S) and then oxidized upon exposure to air. This interpretation is substantiated by linear combination analyses performed in both the XANES and EXAFS regions, where Type OS spectra match a partially oxidized Type S spectrum with $\sim$60% of the Mo in the form of the air-oxidized Type S sample (Y) and $\sim$40% in the form of the original anoxic Type S (Table 6). Further, both Type S and Type OS samples react to form compounds with identical XAFS spectra upon further oxidation and drying (CDP6-Y match CDP9-Y) and oxidation and combustion (CDP6-Z match CDP9-Z).

Oxidation most likely occurred during analysis at the beamline or during formation in the lake ($\sim$700–3500 cal yr BP) and not during sampling or handling where great care was taken to avoid exposure to O_2. If oxidation in Type OS samples took place in the lab, it would likely have occurred during the $\sim$3 h of analysis at the beamline when the mud was protected from ambient air only with a layer of Lexan and Kapton tape. In any case, we conclude that Mo(IV)–S

Table 7
Comparison of bonding environments in natural and laboratory experiments for simple best fit EXAFS models.

	Cadagno Type S	Cadagno Type OS (partly oxidized)	Cadagno Y 70 °C + oxidized	Black Shales	MoS_4^{2-}–FeS_2 adsorbate	Mo–Fe–S cubane in Cp1[1]	MoS_3
Mo–O	None	1.69–1.74	1.74–1.78	1.69–1.71	1.76–1.78	None	None
Mo–S	2.24–2.38	2.29–2.36	2.37–2.38	2.31–2.38	2.39–2.41	2.35 ± 0.03 (3–4) 2.49 ± 0.03 (1–2)	2.43
Mo–Fe	2.71–2.73	2.73–2.77	2.90–2.96	2.60–2.64	2.68–2.72	2.72 ± 0.05 (1)	None
Mo oxid. state	4.3 ± 0.5	5.5 ± 0.5	5.5 ± 0.5	4–6	?	4	4
Reference	(2)	(2)	(2)	(3)	(4)	(5)	(6)

[1] Cp1 = molybdenum–iron (MoFe) protein of *Clostridium pasteurianum* contains two Mo atoms.
[2] This work.
[3] Helz et al. (1996).
[4] Bostick et al. (2003).
[5] Cramer et al. (1978) and Venters et al. (1986).
[6] Hibble et al. (1995).

compounds in euxinic Cadagno sediments are sensitive to O_2 and that Mo–S bonds may be broken within hours of drying and air exposure.

The oxidized Mo compounds compare well to black shales previously described by (Helz et al., 1996) (Table 7), suggesting that their samples also suffered from oxidation. Due to the extreme Mo enrichments (>100 ppm) in the samples of Helz et al., they must have been deposited in an (at least) intermittently sulfidic basin where the euxinic Mo burial pathway produced strong Mo enrichment (Lyons et al., 2009; Scott and Lyons, 2012). Therefore oxidation could have occurred during deposition in association with intermittent O_2 intrusions, perhaps via fluctuations in the position of the chemocline (discussed further below). Alternatively, oxidation was a post-depositional phenomenon, it could have occurred during oxic weathering in outcrop or after sample collection, during preparation or at the beamline during analysis.

4.3. Mo speciation in euxinic sediments

The Mo speciation in euxinic sediments has long been debated. Our data confirm previous interpretations based on several lines of evidence that molybdenite is not the dominant phase (Bostick et al., 2003), hence molybdenite precipitation in euxinic waters and during low-temperature diagenesis can be excluded. The distinct characteristics of our samples include their air sensitivity, Mo–S bond length, and coordination number, all of which point to a predominance of Mo(IV)–S compounds distinct from amorphous or crystalline MoS_2 minerals. For example, Mo–S bond lengths, at 2.24–2.38 Å, are shorter than those in crystalline molybdenite at 2.41 ± 0.01 Å. Amorphous molybdenite would have similar or even longer bond lengths compared to the crystalline forms. Also, our best-fit coordination numbers yield four sulfur ligands (R-factors = 0.03–0.24), in contrast to the six sulfur ligands in molybdenite (R-factors > 0.80 or requiring physically unrealistic parameter values). Further, molybdenite forms impure MoO_3 when roasted in the presence of O_2. In fact, such roasting is the first step in the MoS_2 refining process (Stiefel, 2000). Our

combusted sediments display XANES spectra clearly distinct from MoO_3 (Fig. 5), with more pronounced pre-edges (Fig. 6). Indeed, the short Mo–O bonds at 1.69–1.74 Å are consistent with terminal Mo=O bonds (typically 1.66–1.76 Å) and not the broad range of Mo–O bond lengths known for MoO_3 (from 1.67 to 2.33 Å) (Fig. 7, Table S1). Finally, our linear combination fitting shows that molybdenite is not a major Mo component in the anoxic samples.

The interatomic distances in Type OS samples are similar to experimental products formed when tetrathiomolybdate is scavenged by pyrite (Table 7; Bostick et al., 2003). Bostick et al. analyzed their samples after air exposure of <24 h, suggesting that Mo oxidation with O_2 at the beamline was a factor, as we infer from our oxidation experiments. Our samples contained variable amounts of reducing agents other than Mo (e.g., Fe^{2+} and S^{2-}), and this may have provided some O_2 buffering capacity and thus protection against oxidation in Type S samples. Hence, if we accept that Mo oxidation took place in both our Type OS samples and the materials analyzed by Bostick et al., then our spectral data from euxinic Lake Cadagno do not rule out the possibility that Mo is scavenged with pyrite, but the environmental context does. Specifically, the Mo(IV)–S compounds in SC1-X formed at or above the sediment-water interface where pyrite is absent and only amorphous FeS precipitates (Dahl et al., 2010a). Mo release and re-adsorption onto pyrite has been suggested to occur at 10–15 cm depth in the sediments (Dahl et al., 2010a), but our spectral data are too sparse to support firm conclusions about any possible molecular transformations during this process. In any case, the main removal mechanism(s) for dissolved Mo in the water column and at the sediment-water interface would take place via amorphous FeS or mackinawite and/or organic matter and not with pyrite. Laboratory experiments have confirmed that thiomolybdate is removed onto freshly precipitated FeS phases (Helz et al., 2004). Furthermore, Helz et al. (2011) posited, based on Mo–FeS relationships in natural sulfidic settings that thiomolybdate and FeS reach saturation levels and co-precipitate as a hypothesized $Fe_5Mo_3S_{14}$ phase. There are currently no XAFS spectra from Mo–FeS precipitation

experiments to compare to the Mo-sulfide compounds found in Lake Cadagno.

The exact molecular structure(s) of Mo–S compounds in the euxinic sediments of Lake Cadagno remains elusive because no available reference materials match our spectra. However, a qualitative guess can be made from the Mo bonding environment obtained in our study. The interatomic Mo–S and Mo–Fe distances compare well with the MoFe proteins Avl and Cpl in nitrogen-fixing bacteria *A. vinelandii and C. pasteurianum*, respectively (Fig. 7) (Cramer et al., 1978; Chen et al., 1993). These MoFe proteins are extremely sensitive to O_2 (Cramer et al., 1978); the enzyme is non-functional after 1 minute of atmospheric exposure (Shah and Brill, 1977). Yet, it is not known if oxidation of the MoFe cofactor is causing this malfunction. In this protein, Mo resides in one corner of a cuboidal structure with three to four sulfur ligands at 2.35 ± 0.03 Å, 1–2 S ligands at 2.49 ± 0.03 Å, and 2–3 Fe atoms at 2.72 ± 0.03 Å (Cramer et al., 1978). When active, Mo resides in its +4 oxidation state in the enzyme (Venters et al., 1986), and there are no Mo–O ligands. Because these similarities with our observations in Lake Cadagno are significant, EXAFS spectra of the Type S samples were compared to theoretical EXAFS model spectra for the proteins based on the fixed bond lengths and the number of ligands as given above. The nitrogenase Mo–S–Fe configuration gave acceptable Debye Waller factors, global amplitude terms, and zero-point energies for type S spectra with excellent goodness of fit (R_R-factors = 0.04–0.09, Table S3). In fact, fits were better than those obtained for our reference materials. Hence, we conclude that the Mo phase(s) in our natural euxinic sediments is, based on this XAFS analysis, indistinguishable from the Mo–Fe–S cubane found in nitrogenase enzymes and generally more similar to this compound than to MoS_2. That said, the observed Mo compounds do not derive from nitrogenase produced by diazotrophs in the lake. The Mo/C ratio in diazotrophs ($<0.5 \times 10^{-4}$ by atoms, Tuit et al., 2004) is significantly lower than in the euxinic sediments ($>1 \times 10^{-4}$, Dahl et al., 2010a). Hence, the majority of Mo in our samples are derived from another enrichment process.

4.4. Chemical burial pathway from water to sediments

A mechanism for the reduction step as part of the Mo burial pathway from sulfidic waters to the sediments has been proposed but is seldom discussed in the modern or paleo-environmental literature (Vorlicek et al., 2004). In this scheme, Mo reduction takes place following the formation of thiomolybdate via reactions with zero-valent sulfur. Where H_2S_{aq} levels exceed 11 μM molybdate is no longer stable and reacts to form tetra-thiomolybdate ($[H_2S_{aq}] = K_{04}^{-1/4} = 11$ μM; Erickson and Helz, 2000). These sulfidation reactions are partly interrupted when tri-thiomolybdate starts to form, because S_8 attacks $MoOS_3^{2-}$ to form polysulfide rings (a process that surprisingly was not observed on MoS_4^{2-}; Vorlicek et al., 2004). The reduced S ligands re-arrange and cause Mo reduction with concomitant oxidation of S to form $Mo(IV)X(S_4)S^{2-}$ or perhaps $Mo(V)_2X_2S_{5+n}^{2-}$ dimers, where n is an integer,

and X is either O or S. These reduced Mo–S species were rapidly scavenged on pyrite in controlled laboratory experiments – whereas tetrathiomolybdate itself was not efficiently scavenged (Vorlicek et al., 2004). In a previous study (Bostick et al., 2003), XAFS spectra were obtained for these same experimental products, and an analog compound structure similar to Mo–Fe–S cubane in the FeMo cofactor in nitrogenase was inferred (Cramer et al., 1978). Our new data strengthen this view and highlight the likelihood that Mo–O ligands in Bostick et al.'s compounds formed as a result of exposure to air.

Therefore, laboratory and field-based studies are now beginning to converge on at least one of the plausible, consistent chemical reaction pathways for Mo burial in euxinic sediments. In this view, Mo is transported in oxic waters as soluble MoO_4^{2-}. When molybdate enters sulfidic waters with >11 μM H_2S (Erickson and Helz, 2000; Zheng et al., 2000), the Mo=O double bonds break in a series of sulfidation reactions to form Mo=S in thiomolybdates, $MoO_{4-x}S_x^{2-}$, which would eventually generate MoS_4^{2-} (Erickson and Helz, 2000). Zero-valent sulfur present in natural sulfidic waters (Zopfi et al., 2001; Wang and Tessier, 2009) breaks the sulfur double bonds in $MoOS_3^{2-}$ (but apparently not in MoS_4^{2-}) to produce a polysulfide ring that induces a ligand-promoted reduction and the formation of highly reactive $Mo(IV)X(S_4)S^{2-}$ (Vorlicek et al., 2004). These Mo(IV)-polysulfide compounds are readily scavenged with amorphous FeS and could form the Mo–Fe–S cubanes that we infer are deposited at the sediment-water interface. This set of reactions seems sufficient to explain the conversion from unreactive Mo to highly reactive Mo–sulfide phases and thus could contribute to, if not dominate, the strong Mo enrichments in at least some euxinic sediments. We note, however, that the post-Mo-polysulfide reactions and, specifically, the role of organic matter are still left unexplained.

Mo correlates to total organic carbon content in the drill core (Wirth et al., 2012). However, the linkage between Mo and organic C is not directly observed in this study because data quality limited our ability to study the coordination environment beyond the second or third shell of atoms from Mo. Hence, there would be no spectral differences whether or not the Mo–Fe–S cubanes were hosted in an organic matrix. The oxidation and combustion treatment at 700 °C shows evidence that an endothermic reaction is breaking the bridging Mo–O ligands to form new Mo=O bonds. We can speculate that this occurs as the organic matrix to which Mo is linked via S and Fe is decomposed.

4.5. Geochemical implications for the Mo-based paleo-proxies

The reduced Mo–S compounds are preserved both at the sediment-water interface and at 8–9 m depth, and there are no systematic differences in oxidation state with depth, which argues against a diagenetic origin for these phases (Fig. 8). All samples contain strong enrichments (19–197 ppm) relative to catchment rocks, suggesting authigenic Mo delivery to the sediments via a sulfidic Mo removal pathway. Some Type OS samples show muted enrichments
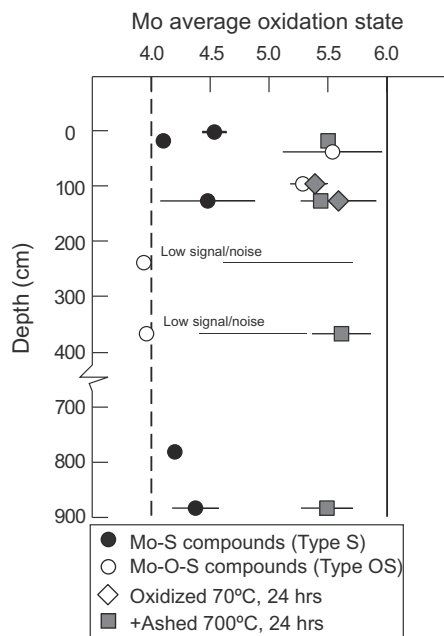
Fig. 8. Depth profile showing our estimated average Mo oxidation state in sediments from Lake Cadagno drill core. Errors estimates are described in the text and in caption of Table 4. Sedimentological descriptions are summarized in Table 2 and in the Supplementary information (after Wirth et al. 2012).

(19–38 ppm), while others are highly enriched (120–190 ppm), which is consistent with the sedimentological evidence for mass movement in one case (CDP20), if delivered from the Mo-poor oxic zone. However, this cannot explain the other three Type OS samples. The simplest explanation is that Mo(IV)–S compounds (Type S) have formed continuously in Lake Cadagno via the same chemical reaction pathway over the last ~9800 years. Oxidized Mo–O -S (Type OS) compounds were found at intermediate depths in the core and might reflect post-depositional oxidation during XAFS analysis or a more oxidative chemical burial pathway during this period of deposition. Consequently, the Mo–S phase (Type S) is stable, when protected from oxygen exposure, during later diagenesis even after H_2S has reacted out of the pore fluids (Dahl et al., 2010a).

Seasonal hypoxia is known to occur in many coastal regions worldwide (Diaz and Rosenberg, 2008). During these anoxic events, hydrogen sulfide (and elemental sulfur) can be present in the hypolimnion and promote thiomolybdate formation (with H_2S), thiomolybdate reduction (with S_8), and precipitation of Mo–Fe–S phases (with FeS and likely organic matter). Yet, we emphasize that the role of hydrogen sulfide is critical. H_2S_{aq} is a necessary prerequisite whereas higher zero-valent sulfur concentrations only enhance the relative proportion of (highly particle reactive) Mo(IV)–sulfide species vs. (less reactive or unreactive) thiomolybdate species. We speculate that the O_2-sensitivity of the Mo–Fe–S compounds in Cadagno sediments affects the solubility of the Mo compounds. This could potentially cause oxidative dissolution of Mo at the sediment surface. Modern intermittently euxinic/anoxic sediments off the

coast of Namibia and Peru (Weeks et al., 2004; Lavik et al., 2009) display strong Mo enrichments (~60 ppm; Brongersma-Sanders et al., 1980; Böning et al., 2004), but generally lower than in permanently euxinic sediments (Scott and Lyons, 2012). Oxidative dissolution may also occur in the Mo-poor sediments of the seasonally anoxic Chesapeake Bay sediments where concentrations remain around crustal levels, only ~1 ppm (Scheiderich et al., 2010).

Unraveling the role of a zero-valent sulfur donor (e.g., S_8) during Mo accumulation in euxinic settings may improve our ability to infer past seawater Mo concentrations from the sedimentary record. Currently, Mo/TOC ratios in modern euxinic environments are used as a proxy for the Mo abundance in the overlying water column (Algeo and Lyons, 2006), and these estimates can provide key information about the global oxygenation state of the ocean in the past (Scott et al., 2008; Dahl et al., 2011). However, as we show here, other controls are also important. For example, Mo/TOC in Black Sea sediments is threefold higher (15 ppm/wt%) at 400 m depth immediately below the 11 μM H_2S_{aq} threshold compared to the deepest part of the basin (5 ppm/wt%) (Brumsack, 1989; Crusius et al., 1996; Nägler et al., 2005; Neubert et al., 2008). Although data are not available from 400 m depth, zero-valent sulfur data from the Black Sea water column shows a peak near the O_2/H_2S chemocline at ~100 m depth and is expected to be more readily available in the upper reaches of the euxinic water column in general (Jørgensen et al., 1991). The lower Mo/TOC and slower Mo accumulation rate at greater depths compared to immediate depths may point to the importance of zero-valent sulfur during Mo uptake in the Black Sea. Also, we speculate that oxygen intrusions into the deep part of some basins – e.g., the Cariaco basin (Scranton et al., 2001), or considerable fluctuations of the chemocline in less stably stratified basins (e.g., 150–238 m in Saanich Inlet) – would cause partial oxidation of dissolved sulfide, yielding zero-valent S. The zero-valent S then reacts with thiomolybdate to form highly reactive Mo-polysulfides that readily adsorb onto settling particles. This could mean that Mo accumulation rate is higher in intermediately sulfidic settings (where S_8 is available) relative to more sulfidic settings where S_8 is scarce.

Strong Mo enrichments of more than ~25 ppm in organic-rich sediments, often much greater, are indicative of euxinic deposition (Lyons et al., 2009; Scott and Lyons, 2012), and values at the lower end of this spectrum and even lower are expected at times when euxinic oceans were greatly expanded and exhausted the seawater Mo inventory (Anbar et al., 2007; Scott et al., 2008; Dahl et al., 2011). Thus, Mo inventory – local and global – is an important control on Mo enrichment. However, the Mo proxy is particularly sensitive to how well we understand the enrichment processes, including controls in addition to dissolved Mo concentration and the presence and amount of dissolved sulfide. These factors include the roles of organic and FeS phases and the relationships to sulfide oxidation that we propose here. Collectively, these various factors add up to yield pronounced Mo enrichments in modern euxinic environments (Lyons et al., 2009), but it will be

important to consider how all these factors line up through geologic time in various supporting and offsetting ways. For example, Mo enrichments are significantly lower (e.g., 3–25 ppm) in euxinic sediments formed in the Precambrian oceans (Scott et al., 2008; Dahl et al., 2010b) compared to those observed today. Beyond lower Mo availability in the ocean, sulfate levels were also much lower (Shen et al., 2002; Johnston et al., 2010), which could have impacted the availability of H_2S and intermediate S forms that facilitate Mo uptake (Erickson and Helz, 2000; Vorlicek et al., 2004). Also, less O_2 in the ocean might have resulted in less S oxidation in the ocean.

In summary, we have documented a reduction step involved in the Mo removal process following the formation of thiomolybdate and refer to laboratory experiments showing that zero-valent sulfur is one key factor in reducing thiomolybdate and producing highly reactive Mo(IV)–S phases (Vorlicek et al., 2004), which are readily scavenged from the sulfidic water column or at the euxinic sediment-water interface. Importantly, Mo reduction occurs with thiomolybdates ($MoOS_3^{2-}$, and perhaps $MoO_2S_2^{2-}$) and is favored by H_2S_{aq} concentrations >11 μM, because this level of sulfide is required to sustain the sulfidation reaction of molybdate and produce softer Mo=S ligands susceptible to reduction (Erickson and Helz, 2000). Hence, this mechanism is not expected to operate in permanently low sulfide sediments with O_2 in the overlying water but may well occur in highly sulfidic sediments even with O_2 in the overlying water column.

5. CONCLUSIONS

The main conclusions of this study are as follows:

1. Mo is reduced in a naturally euxinic environment and predominantly forms Mo(IV)–S compound(s), distinct from molybdenite, implying that the post-thiomolybdate steps of the Mo burial pathway involves a reduction step in euxinic Lake Cadagno. This is in agreement with observations made in ancient shales (Helz et al., 1996).
2. XAFS evidence for the same molecular structures were found in core samples in both recent and ~9800 years old sediments, suggesting little post-deposition chemical transformation, such as diagenetic molybdenite formation. Hence, bulk Mo isotope compositions in euxinic sediments should preserve a signature of water column processes.
3. Upon air exposure, the predominant Mo(IV)–S in modern sediments form Mo(VI)–O, and the oxidized compounds are comparable to ancient black shales previously described by Helz et al. (1996), suggesting that the ancient samples may have experienced oxidation, either in nature, during lab storage, or over the course of that research. Hence, the potential artifacts introduced by this oxidation process must be considered in future studies of Mo enrichment mechanisms.
4. The derived molecular structure of the pristine Mo(IV)–S (Type S) compounds does not match any of our isolated reference compounds, but the immediate coordination environment, Mo oxidation state, and its oxygen

sensitivity are features shared with the Mo–Fe–S cubane found in Mo-nitrogenase enzyme (as an analog compound, but nitrogenase is not the main carrier of Mo in the sediments). A theoretical EXAFS model for Mo–Fe–S cubane confirms this prediction with a goodness of fit (R-factor) better than those obtained for known reference materials using our fitting procedure.
5. Zero-valent sulfur may play a crucial role in the Mo burial processes occurring within sulfidic settings and accelerate the Mo accumulation rate in euxinic basins where oxygen intrudes at depth, like in Cariaco Basin. This new insight should have consequences for effective and refined use of Mo as a paleo-redox proxies; i.e., including its isotopes.
6. XAFS measurements of geological samples can provide key information on the coordination chemistry of elements used as paleoproxies and constrain their redox states in the depositional environment.

APPENDIX A. SUPPLEMENTARY DATA

Supplementary data associated with this article can be found, in the online version, at http://dx.doi.org/10.1016/j.gca.2012.10.058.

REFERENCES

Algeo T. J. and Lyons T. W. (2006) Mo–total organic carbon covariation in modern anoxic marine environments: Implications for analysis of paleoredox and paleohydrographic conditions. *Paleoceanography* **21**, 1–23.

Anbar A. D., Duan Y., Lyons T. W., Arnold G. L., Kendall B., Creaser R. A., Kaufman A. J., Gordon G. W., Scott C., Garvin J. and Buick R. (2007) A whiff of oxygen before the great oxidation event? *Science* **317**, 1903–1906.

Arnold G. L., Anbar A. D., Barling J. and Lyons T. W. (2004) Molybdenum isotope evidence for widespread anoxia in mid-proterozoic oceans. *Science* **304**, 87–90.

Bianconi A. (1988) XANES spectroscopy. In *X-ray Absorption – Principles, Applications and Techniques of EXAFS, SEXAFS*

and XANES (eds. D. Konigsberger and R. Prins). John Wiley & Sons, Inc..

Böning P., Brumsack H.-J., Böttcher M. E., Schnetger B., Kriete C., Kallmeyer J. and Borchers S. L. (2004) Geochemistry of Peruvian near-surface sediments. *Geochim. Cosmochim. Acta* **68**, 4429–4451.

Bostick B. C., Fendorf S. and Helz G. R. (2003) Differential adsorption of molybdate and tetrathiomolybdate on pyrite (FeS₂). *Environ. Sci. Technol.* **37**, 285–291.

Brongersma-Sanders M., Stephan K. M., Kwee T. G. and De Bruin M. (1980) Distribution of minor elements in cores from the Southwest Africa shelf with notes on plankton and fish mortality. *Mar. Geol.* **37**, 91–132.

Brumsack H. J. (1989) Geochemistry of recent TOC-rich sediments from the Gulf of California and the Black Sea. *Geol. Rundsch.* **78**, 851–882.

Calvert S. E. and Pedersen T. F. (1993) Geochemistry of recent oxic and anoxic marine sediments: implications for the geological record. *Mar. Geol.* **113**, 67–88.

Chappaz A., Gobeil C. and Tessier A. (2008) Geochemical and anthropogenic enrichments of Mo in sediments from perennially oxic and seasonally anoxic lakes in Eastern Canada. *Geochim. Cosmochim. Acta* **72**, 170–184.

Chen J., Christiansen J., Tittsworth R., Hales B., George S., Coucouvanis D. and Cramer S. (1993) Iron EXAFS of *Azotobacter vinelandii* nitrogenase molybdenum–iron and vanadium–iron proteins. *J. Am. Chem. Soc.* **115**, 5509–5515.

Cramer S. P., Hodgson K. O., Gillum W. O. and Mortenson L. E. (1978) Molybdenum site of nitrogenase – preliminary structural evidence from X-ray absorption spectroscopy. *J. Am. Chem. Soc.* **100**, 3398–3407.

Cramer S. P., Liang K. S., Jacobson A. J., Chang C. H. and Chianelli R. R. (1984) EXAFS studies of amorphous molybdenum and tungsten trisulfides and triselenides. *Inorg. Chem.* **23**, 1216–1221.

Crusius J., Calvert S., Pedersen T. and Sage D. (1996) Rhenium and molybdenum enrichments in sediments as indicators of oxic, suboxic and sulfidic conditions of deposition. *Earth Planet. Sci. Lett.* **145**, 65–78.

Dahl T. W., Anbar A. D., Gordon G. W., Rosing M. T., Frei R. and Canfield D. E. (2010a) The behavior of molybdenum and its isotopes across the chemocline and in the sediments of sulfidic Lake Cadagno, Switzerland. *Geochim. Cosmochim. Acta* **74**, 144–163.

Dahl T. W., Canfield D. E., Rosing M. T., Frei R. E., Gordon G. W., Knoll A. H. and Anbar A. D. (2011) Molybdenum evidence for expansive sulfidic water masses in ∼750 Ma oceans. *Earth Planet. Sci. Lett.* **311**, 264–274.

Dahl T. W., Hammarlund E. U., Anbar A. D., Bond D. P. G., Gill B. C., Gordon G. W., Knoll A. H., Nielsen A. T., Schovsbo N. H. and Canfield D. E. (2010b) Devonian rise in atmospheric oxygen correlated to the radiations of terrestrial plants and large predatory fish. *Proc. Nat. Acad. Sci.* **107**, 17911–17915.

Del Don C., Hanselmann K. W., Peduzzi R. and Bachofen R. (2001) The meromictic alpine Lake Cadagno: orographical and biogeochemical description. *Aquat. Sci.* **63**, 70–90.

Diaz R. J. and Rosenberg R. (2008) Spreading dead zones and consequences for marine ecosystems. *Science* **321**, 926–929.

Dickinson R. G. and Pauling L. (1923) The Crystal Structure of molybdenite. *J. Am. Chem. Soc.* **45**, 1466–1471.

Emerson S. and Huested S. S. (1991) Ocean anoxia and the concentrations of molybdenum and vanadium in seawater. *Mar. Chem.* **34**, 177–196.

Erickson B. E. and Helz G. R. (2000) Molybdenum(VI) speciation in sulfidic waters: stability and lability of thiomolybdates. *Geochim. Cosmochim. Acta* **64**, 1149–1158.

Francois R. (1988) A study on the regulation of the concentrations of some trace metals (Rb, Sr, Zn, Pb, Cu, V, Cr, Ni, Mn and Mo) in Saanich Inlet Sediments, British Columbia, Canada. *Mar. Geol.* **83**, 285–308.

Helz G. R., Bura-Nakić E., Mikac N. and Ciglenečki I. (2011) New model for molybdenum behavior in euxinic waters. *Chem. Geol.* **284**, 323–332.

Helz G. R., Miller C. V., Charnock J. M., Mosselmans J. F. W., Pattrick R. A. D., Garner C. D. and Vaughan D. J. (1996) Mechanism of molybdenum removal from the sea and its concentration in black shales: EXAFS evidence. *Geochim. Cosmochim. Acta* **60**, 3631–3642.

Helz G. R., Vorlicek T. P. and Kahn M. D. (2004) Molybdenum scavenging by iron monosulfide. *Environ. Sci. Technol.* **38**, 4263–4268.

Hibble S. J., Rice D. A., Pickup D. M. and Beer M. P. (1995) Mo K-edge EXAFS and S K-edge absorption studies of the amorphous molybdenum sulfides MoS4.7, MoS3, and MoS3.nH2O (n ∼ 2). *Inorg. Chem.* **34**, 5109–5113.

Johnston D. T., Poulton S. W., Dehler C., Porter S., Husson J., Canfield D. E. and Knoll A. H. (2010) An emerging picture of neoproterozoic ocean chemistry: Insights from the Chuar Group, Grand Canyon, USA. *Earth Planet. Sci. Lett.* **290**, 64–73.

Jørgensen B. B., Fossing H., Wirsen C. O. and Jannasch H. W. (1991) Sulfide oxidation in the anoxic Black Sea chemocline. *Deep Sea Res. Part I* **38**, S1083–S1103.

Knox J. and Prout C. (1969) The structure of a cysteine complex of molybdenum (V): Na₂Mo₂O₄[SCH₂CH(NH₂)CO₂]·2.5H₂O. *Acta Crystallogr. B: Struct. Crystallogr. Cryst. Chem.* **25**, 1857–1866.

Lapasset J., Chezau N. and Belougne P. (1976) Nouvel affinement de la structure cristalline du thiomolybdate d'ammonium. *Acta Crystallogr. B: Struct. Crystallogr. Cryst. Chem.* **32**, 3087–3088.

Lavik G., Stuhrmann T., Bruchert V., Van der Plas A., Mohrholz V., Lam P., Mussmann M., Fuchs B. M., Amann R., Lass U. and Kuypers M. M. (2009) Detoxification of sulphidic African shelf waters by blooming chemolithotrophs. *Nature* **457**, 581–584.

Lyons T. W., Anbar A. D., Severmann S., Scott C. and Gill B. C. (2009) Tracking euxinia in the ancient ocean: a multiproxy perspective and proterozoic case study. *Annu. Rev. Earth Planet. Sci.* **37**, 507–534.

Miller C. A., Peucker-Ehrenbrink B., Walker B. D. and Marcantonio F. (2011) Re-assessing the surface cycling of molybdenum and rhenium. *Geochim. Cosmochim. Acta* **75**, 7146–7179.

Morford J. L. and Emerson S. (1999) The geochemistry of redox sensitive trace metals in sediments. *Geochim. Cosmochim. Acta* **63**, 1735–1750.

Morford J. L., Martin W. R., Kalnejais L. H., François R., Bothner M. and Karle I.-M. (2007) Insights on geochemical cycling of U, Re and Mo from seasonal sampling in Boston Harbor, Massachusetts, USA. *Geochim. Cosmochim. Acta* **71**, 895–917.

Nägler T. F., Siebert C., Lüschen H. and Böttcher M. E. (2005) Sedimentary Mo isotope record across the Holocene fresh-brackish water transition of the Black Sea. *Chem. Geol.* **219**, 283–295.

Neubert N., Nägler T. F. and Böttcher M. E. (2008) Sulfidity controls molybdenum isotope fractionation into euxinic sediments: evidence from the modern Black Sea. *Geology* **36**, 775–778.

Pearce C. R., Cohen A. S., Coe A. L. and Burton K. W. (2008) Molybdenum isotope evidence for global ocean anoxia coupled with perturbations to the carbon cycle during the Early Jurassic. *Geology* **36**, 231–234.

Ravel B. and Newville M. (2005) ATHENA, ARTEMIS, HEPHAESTUS: data analysis for X-ray absorption spectroscopy using IFEFFIT. *J. Synchrotron Radiat.* **12**, 537–541.

Rehr J. J. and Albers R. C. (2000) Theoretical approaches to X-ray absorption fine structure. *Rev. Mod. Phys.* **72**, 621–654.

Ressler T. (2000) Time-resolved XAS investigation of the reduction/oxidation of $MoO_{3−x}$. *J. Catal.* **191**, 75–85.

Ressler T. (2002) Bulk structural investigation of the reduction of MoO_3 with propene and the oxidation of MoO_2 with oxygen. *J. Catal.* **210**, 67–83.

Scheiderich K., Helz G. R. and Walker R. J. (2010) Century-long record of Mo isotopic composition in sediments of a seasonally anoxic estuary (Chesapeake Bay). *Earth Planet. Sci. Lett.* **289**, 189–197.

Scott C. and Lyons T. W. (2012) Contrasting molybdenum cycling and isotopic properties in euxinic versus non-euxinic sediments and sedimentary rocks: refining the paleoproxies. *Chem. Geol.* **324–325**, 19–21.

Scott C., Lyons T. W., Bekker A., Shen Y., Poulton S. W., Chu X. and Anbar A. D. (2008) Tracing the stepwise oxygenation of the Proterozoic ocean. *Nature* **452**, 456–459.

Scranton M. I., Astor Y., Bohrer R., Ho T.-Y. and Muller-Karger F. (2001) Controls on temporal variability of the geochemistry of the deep Cariaco Basin. *Deep Sea Res. Part I* **48**, 1605–1625.

Shah V. K. and Brill W. J. (1977) Isolation of an iron–molybdenum cofactor from nitrogenase. *Proc. Natl. Acad. Sci. U.S.A.* **74**, 3249–3253.

Shen Y., Canfield D. and Knoll A. (2002) Middle Proterozoic ocean chemistry: evidence from the McArthur Basin, northern Australia. *Am. J. Sci.* **302**, 81–109.

Shimmield G. and Price N. (1986) The behaviour of molybdenum and manganese during early sediment diagenesis offshore Baja California, Mexico. *Mar. Chem.* **19**, 261–280.

Stern E. A. (1988) Theory of EXAFS. In *X-ray Absorption: Principles, Applications, Techniques of EXAFS, SEXAFS and XANES* (eds. D. C. Koningsberger and R. Prins). John Wiley and Sons, New York, pp. 3–51.

Stiefel E. I. (2000). *Molybdenum compounds, Kirk-Othmer Encyclopedia of Chemical Technology*. John Wiley & Sons, Inc..

Tribovillard N., Algeo T. J., Lyons T. and Riboulleau A. (2006) Trace metals as paleoredox and paleoproductivity proxies: an update. *Chem. Geol.* **232**, 12–32.

Tribovillard N., Riboulleau A., Lyons T. and Baudin F. (2004) Enhanced trapping of molybdenum by sulfurized marine organic matter of marine origin in Mesozoic limestones and shales. *Chem. Geol.* **213**, 385–401.

Tuit C., Waterbury J. and Ravizza G. (2004) Diel variation of molybdenum and iron in marine diazotrophic cyanobacteria. *Limno. Oceanogr.* **49**, 978–990.

Venters R. A., Nelson M. J., McLean P. A., True A. E., Levy M. A., Hoffman B. M. and Orme-Johnson W. H. (1986) ENDOR of the resting state of nitrogenase molybdenum-iron proteins from *Azotobacter vinelandii*, *Klebsiella pneumoniae*, and *Clostridium pasteurianum*. Proton, iron-57, molybdenum-95, and sulfur-33 studies. *J. Am. Chem. Soc.* **108**, 3487–3498.

Vorlicek T. P., Kahn M. D., Kasuya Y. and Helz G. R. (2004) Capture of molybdenum in pyrite-forming sediments: role of ligand-induced reduction by polysulfides. *Geochim. Cosmochim. Acta* **68**, 547–556.

Wang D., Aller R. C. and Sañudo-Wilhelmy S. A. (2011) Redox speciation and early diagenetic behavior of dissolved molybdenum in sulfidic muds. *Mar. Chem.* **125**, 101–107.

Wang F. and Tessier A. (2009) Zero-valent sulfur and metal speciation in sediment porewaters of freshwater lakes. *Environ. Sci. Technol.* **43**, 7252–7257.

Weeks S. J., Currie B., Bakun A. and Peard K. R. (2004) Hydrogen sulphide eruptions in the Atlantic Ocean off southern Africa: implications of a new view based on SeaWiFS satellite imagery. *Deep Sea Res. Part I* **51**, 153–172.

Wichard T., Mishra B., Myneni S., Bellenger J. and Kraepiel A. (2009) Storage and bioavailability of molybdenum in soils increased by organic matter complexation. *Nat. Geosci.* **2**, 625–629.

Wille M., Kramers J. D., Nägler T. F., Beukes N. J., Schröder S., Meisel T., Lacassie J. P. and Voegelin A. R. (2007) Evidence for a gradual rise of oxygen between 2.6 and 2.5 Ga from Mo isotopes and Re-PGE signatures in shales. *Geochim. Cosmochim. Acta* **71**, 2417–2435.

Wirth S., Gilli A., Dahl T., Niemann H., Ravasi D., Lehmann M., Peduzzi R., Peduzzi S., Tonolla M. and Anselmetti F. (2012) 9800 Years of meromixis and euxinia in Lake Cadagno (Swiss Alps): sedimentary and biogeochemical evidence for the formation of a permanently stable chemocline. *EGU General Assembly* **2012**, 7395.

Zheng Y., Anderson R. F., van Geen A. and Kuwabara J. (2000) Authigenic molybdenum formation in marine sediments: a link to pore water sulfide in the Santa Barbara Basin. *Geochim. Cosmochim. Acta* **64**, 4165–4178.

Zopfi J., Ferdelman T. G., Jørgensen B. B., Teske A. and Thamdrup B. (2001) Influence of water column dynamics on sulfide oxidation and other major biogeochemical processes in the chemocline of Mariager Fjord (Denmark). *Mar. Chem.* **74**, 29–51.

Associate Editor: Derek Vance